

1 **OH-Initiated atmospheric degradation of hydroxyalkyl**
2 **hydroperoxides: mechanism, kinetics, and structure-activity**
3 **relationship**

4 Long Chen,^{1,2} Yu Huang, ^{*}1,2 Yonggang Xue, ^{1,2} Zhihui Jia, ³ Wenliang Wang⁴

5 ¹ *State Key Lab of Loess and Quaternary Geology (SKLLQG), Institute of Earth*
6 *Environment, Chinese Academy of Sciences (CAS), Xi'an, 710061, China*

7 ² *CAS Center for Excellence in Quaternary Science and Global Change, Xi'an,*
8 *710061, China*

9 ³ *School of Materials Science and Engineering, Shaanxi Normal University, Xi'an,*
10 *Shaanxi, 710119, China*

11 ⁴ *School of Chemistry and Chemical Engineering, Key Laboratory for*
12 *Macromolecular Science of Shaanxi Province, Shaanxi Normal University, Xi'an,*
13 *Shaanxi, 710119, China*

14

15

16

17

18 Submitted to *Atmospheric Chemistry & Physics*

19

20

21 *Corresponding author:

22 Prof. Yu Huang, E-mail address: huangyu@ieecas.cn

23

24 **Abstract:**

25 Hydroxyalkyl hydroperoxides (HHPs), formed in the reactions of Criegee
26 intermediates (CIs) with water vapour, play essential roles in the formation of
27 secondary organic aerosol (SOA) under atmospheric conditions. However, the
28 transformation mechanisms for OH-initiated oxidation of HHPs remain incompletely
29 understood. Herein, the quantum chemical and kinetics modeling methods are applied
30 to insight into the detailed mechanisms of OH-initiated oxidation of distinct HHPs
31 (HOCH₂OOH, HOCH(CH₃)OOH and HOC(CH₃)₂OOH) formed from the reactions of
32 CH₂OO, *anti*-CH₃CHOO and (CH₃)₂COO) with water vapor. The calculations show
33 that the dominant pathway is the H-abstraction from the -OOH group in the initiation
34 reactions of OH radical with HOCH₂OOH and HOC(CH₃)₂OOH. H-abstraction from
35 the -CH group is competitive with that from the -OOH group in the reaction of OH
36 radical with HOCH(CH₃)OOH. The barrier of H-abstraction from the -OOH group is
37 slightly increased as the number of methyl group is increased. In pristine
38 environments, the self-reaction of RO₂ radical initially produces tetroxide
39 intermediate via an oxygen-to-oxygen coupling, then it decomposes into propagation
40 and termination products through the asymmetric two-step O-O bond scission, in
41 which the rate-limiting step is the first O-O bond cleavage. The barrier height of
42 distinct RO₂ radical reactions with HO₂ radical is independent on the number of
43 methyl substitution. In urban environments, reaction with O₂ forming formic acid and
44 HO₂ radical is the dominant removal pathway for HOCH₂O radical formed from the
45 reaction of HOCH₂OO radical with NO. The β-site C-C bond scission is the dominant
46 pathway in the dissociation of HOCH(CH₃)O and HOC(CH₃)₂O radicals formed from
47 the reactions of NO with HOCH(CH₃)OO and HOC(CH₃)₂OO radicals. These new
48 findings are expected to deepen our current understanding for the photochemical
49 oxidation of hydroperoxides under realistic atmospheric conditions.

50

51 **1. Introduction**

52 Hydroxyalkyl hydroperoxides (HHPs), formed in the reactions of Criegee
53 intermediates (CIs) with water vapour and in the initiation OH-addition with
54 subsequent HO₂-termination reactions, play important roles in the formation of
55 secondary organic aerosol (SOA) (Qiu et al., 2019; Kumar et al., 2014). The CIs
56 formed from the ozonolysis of alkenes are characterized by high reactivity and excess
57 energies, which can proceed either prompt unimolecular decay to OH radical or, after
58 collisional stabilization, bimolecular reactions with various trace gases like SO₂,
59 NO₂ and H₂O to produce sulfate, nitrate and SOA, thereby influencing air quality and
60 human health (Lester and Klippenstein, 2018; Chen et al., 2017, 2019; Liu et al., 2019;
61 Chhantyal-Pun et al., 2017; Anglada and Solé 2016; Gong and Chen, 2021). Among
62 these reactions, the bimolecular reaction of CIs with water is thought to be the
63 dominant chemical sink because its concentration ($1.3\text{-}8.3 \times 10^{17}$ molecules cm⁻³) is
64 several orders of magnitude greater than those of SO₂ and NO₂ ($\sim 10^{12}$ molecules cm⁻³)
65 in the atmosphere (Huang et al., 2015; Khan et al., 2018; Taatjes et al., 2013, 2017).
66 The primary products of CIs reactivity toward water are highly oxygenated HHPs that
67 are difficult to detect and identify by using the available analytical techniques due to
68 their thermally instability (Qiu et al., 2019; Anglada and Solé 2016; Chao et al., 2015;
69 Chen et al., 2016a; Ryzhkov and Ariya, 2003).

70 HHPs, due to the presence of both hydroxyl and perhydroxy moieties, have
71 relatively low volatility contributing substantially to the formation of SOA (Qiu et al.,
72 2019). The atmospheric degradation of HHPs initiated by OH radical is expected to be
73 one of the dominant loss processes because OH radical is the most powerful oxidizing
74 agent (Gligorovski et al., 2015; Allen et al., 2018). Reaction with OH radical includes
75 three possible H-abstraction channels: (a) the alkyl hydrogen, (b) the -OH hydrogen,
76 and (c) the -OOH hydrogen, which is followed by further reactions to generate
77 organic peroxy radicals (RO₂) as reactive intermediates (Allen et al., 2018). Based on
78 our current mechanistic understanding, RO₂ radicals have three possible channels in
79 pristine environments: (1) they can proceed self- and cross-reactions resulting in

80 formation of alkoxy radical RO, alcohol, carbonyl, accretion products (Berndt et al.,
81 2018; Zhang et al., 2012; Valiev et al., 2019); (2) they can react with HO₂ radical
82 leading to the formation of closed-shell hydroperoxide (ROOH), RO radical, OH
83 radical, etc.; (Dillon and Crowley, 2008; Iyer et al., 2018) (3) they can undergo
84 autoxidation via intramolecular H-shift and alternating O₂-addition steps producing
85 highly oxygenated organic molecules (HOMs), which have been identified as the low
86 volatility compounds that contribute to the formation of SOA (Crouse et al., 2013;
87 Jokinen et al., 2014; Wang et al., 2018; Ehn et al., 2014; Iyer et al., 2021). In urban
88 environments, RO₂ radicals can react with NO_x generating peroxyxynitrate (RO₂NO₂),
89 organic nitrate (RONO₂), RO radical and other SOA precursors (Wang et al., 2017;
90 Xu et al., 2014, 2020; Ma et al., 2021). The relative importance of distinct pathways
91 depends strongly on the nature of RO₂ radicals and the concentrations of coreactants.

92 Hydroxymethyl hydroperoxide (HMHP, HOCH₂OOH), the simplest HHPs come
93 from the ozonolysis of all terminal alkenes in the presence of water, is observed in
94 significant abundance in the atmosphere (Allen et al., 2018). The measured
95 concentration of HMHP is varied considerably depending on the location, season and
96 altitude, and its concentration is measured to be up to 5 ppbv in forested regions
97 (Allen et al., 2018; Francisco and Eisfeld, 2009). Recently, the concentration of
98 HMHP was measured during the summer 2013 in the southeastern United States, and
99 found that the average mixing ratio of HMHP is 0.25 ppbv with a maximum of 4.0
100 ppbv in the boundary layer (Allen et al., 2018). Allen et al. (2018) conducted the
101 OH-initiated oxidation of HMHP in an environmental chamber and simulated the
102 impact of HMHP oxidation on the global formic acid concentration using the
103 chemical transport model GEOS-Chem. It was found that H-abstraction from the
104 methyl group of HMHP results in formic acid, and it contributes to the global formic
105 acid production about 1.7 Tg yr⁻¹. Francisco and Eisfeld (2009) by employing *ab*
106 *initio* CCSD(T)//MP2 methods, studied the atmospheric oxidation mechanism of
107 HMHP initiated by OH radical, arriving at the same conclusion that the degradation of
108 HMHP could be a new source of formic acid in the atmosphere. Additionally, the
109 unimolecular decomposition of HMHP is another important removal process in the

110 atmosphere. Chen et al. (2016b) found that the formation of CH_2O and H_2O_2 is more
111 preferable than the production of HCOOH and H_2O . Kumar et al. (2014) obtained the
112 same conclusion that the aldehyde- or ketone-forming pathway is kinetically favored
113 over that the carboxylic acid-forming channel in the unimolecular decomposition of a
114 variety of HHPs. All the above milestone investigations offer very useful information
115 for understanding the decomposition of HHPs in the gas phase. However, to the best
116 of our knowledge, there are few studies on the subsequent transformations of the
117 resulting H-abstraction products formed from the OH-initiated oxidation of larger
118 HHPs. The effect of the size and number of substituents on the rates and outcomes of
119 SOA precursors (e.g. ROOR, HOMs) is uncertain up to now. Therefore, it is necessary
120 to assess the potential of larger HHPs and their oxidation products to substantial SOA
121 formation under different NO_x conditions.

122 In this article, we mainly investigate the detailed mechanisms and kinetic
123 properties of distinct HHPs oxidation initiated by OH radical by employing quantum
124 chemical and kinetics modeling methods. For the resulting H-abstraction products
125 RO_2 radicals, the subsequent reactions involving self-reaction, isomerization and
126 reaction with HO_2 radical are taken into account in the absence of NO , while the
127 subsequent reactions including addition, decomposition and H-abstraction by O_2 are
128 considered in the presence of NO . The investigated HHPs in this work are generated
129 from the bimolecular reactions of distinct carbonyl oxides (CH_2OO , *anti*- CH_3CHOO
130 and $(\text{CH}_3)_2\text{COO}$) with water vapor.

131 **2. Computational details**

132 **2.1 Electronic structure and energy calculations**

133 The equilibrium geometries of all the open-shell species, including reactant (R),
134 pre-reactive complex (RC), transition state (TS), post-reactive complex (PC), and
135 product (P), are fully optimized at the unrestricted M06-2X/6-311+G(2df,2p) level of
136 theory (UM06-2X) (Zhao and Truhlar, 2006; Zheng and Truhlar, 2009), whereas all
137 the closed-shell species are optimized at the restricted M06-2X/6-311+G(2df,2p) level
138 of theory (RM06-2X). This is because the M06-2X functional has been proven to

139 produce reliable performance for describing thermochemistry, kinetics and
140 non-covalent interactions (Zhao and Truhlar, 2008). Harmonic vibrational frequencies
141 are performed at the same level to verify that each stationary point is either a true
142 minima (with no imaginary frequency) or a transition state (with one imaginary
143 frequency). Zero-point vibrational energy (ZPVE) and Gibbs free energy corrections
144 (G_{corr}) from harmonic vibrational frequencies are scaled by a factor of 0.98 (Zhao and
145 Truhlar, 2006). The intrinsic reaction coordinate (IRC) calculations are performed to
146 verify the connection between the transition state and the designated reactant and
147 product (Fukui, 1981). The single-point energies are calculated at the
148 (U/R)M06-2X/ma-TZVP level of theory (Zheng, et al., 2011).

149 The tetroxide intermediate formed from the self-reaction of RO_2 radical proceeds
150 through the asymmetric two step O-O bond scission to produce a caged tetroxide
151 intermediate of overall singlet multiplicity comprising two same-spin alkoxy radicals
152 (spin down) and triplet oxygen (spin up). This type of reaction mechanism can be
153 described by the broken symmetry unrestricted DFT (UDFT) and multi-reference
154 CASSCF methods (Lee, et al., 2016; Bach, et al., 2005). Previous studies have
155 demonstrated that the UDFT method is suitable to identify the minimum of metastable
156 singlet caged radical complex and the transition state of O-O bond homolysis, for
157 which the energies are comparable to the more accurate and expensive CASSCF
158 method (Lee, et al., 2016; Bach, et al., 2005). In the present study, the UDFT method
159 is selected to study the asymmetric O-O bond scission and represents a compromise
160 between the computational accuracy and efficiency. The broken symmetry
161 UM06-2X/6-311+G(2df,2p) method is applied to generate the initial guesses of the
162 tetroxide intermediate and transition state geometries with mixed HOMO and LUMO
163 ($S^2 \approx 1$) by using the guess = mix keyword. The single-point energies are refined at
164 the UM06-2X/ma-TZVP level of theory.

165 In order to further evaluate the reliability of the employed method in predicting
166 reaction mechanism, the single-point energies for all the stationary points involved in
167 the initiation reactions of OH radical with distinct HHPs are recalculated at the
168 (U/R)CCSD(T)/6-311+G(2df,2p) level of theory based on the (U/R)M06-2X

169 optimized geometries. Furthermore, the basis set superposition error (BSSE) is also
170 performed to evaluate the stability of the pre-reactive complexes by employing the
171 counterpoise method (Boys and Bernardi, 1970). For simplicity, no prefix is adopted
172 throughout this article. Herein, the Gibbs free energy (G) for each species is obtained
173 by combining the single-point energy with the Gibbs correction ($G = G_{\text{corr}} + E$). The
174 electronic energy (ΔE_a^\ddagger) and free energy (ΔG_a^\ddagger) barriers are defined as the difference
175 in energy between transition state and pre-reactive complex ($\Delta E_a^\ddagger = E_{\text{TS}} - E_{\text{RC}}$ and
176 $\Delta G_a^\ddagger = G_{\text{TS}} - G_{\text{RC}}$). The reaction free energy (ΔG) is referred to the difference in
177 energy between product and reactant ($\Delta G = G_{\text{P}} - G_{\text{R}}$). The calculated ΔE_a^\ddagger and ΔG_a^\ddagger
178 for the initiation H-abstraction pathways are summarized in Table S1. As shown in
179 Table S1, the mean absolute deviations (MADs) of ΔE_a^\ddagger and ΔG_a^\ddagger between
180 CCSD(T)/6-311+G(2df,2p) and M06-2X/ma-TZVP approaches are 0.43 and 0.45
181 kcal mol⁻¹, respectively; the largest deviations of ΔE_a^\ddagger and ΔG_a^\ddagger are 1.2 and 1.1
182 kcal mol⁻¹, respectively. These results reveal that the energies obtained from the
183 M06-2X/ma-TZVP method are in very good accord with those from the gold-standard
184 coupled-cluster approach CCSD(T) within the uncertainties of systematic errors.
185 Therefore, the M06-2X/ma-TZVP method is selected to investigate the atmospheric
186 degradation of HHP initiated by OH radical under different conditions. In the
187 following sections, unless otherwise stated, the ΔG_a^\ddagger is applied to construct the
188 reaction profiles.

189 For the H-shift reactions of RO₂ radicals, reactants, transition states and products
190 have multiple conformers. Previous literature has demonstrated that the reaction
191 kinetics of multiconformers involvement are more precisely than that of the single
192 conformer approximation (Møller, et al., 2016, 2020). Herein, the multiconformer
193 treatment is performed to investigate the H-shift reactions of RO₂ radicals. A
194 conformer search within the Molclus program is employed to generate a pool of
195 conformers for RO₂ radicals (Lu, 2020). The selected conformers are further
196 optimized at the M06-2X/6-311+G(2df,2p) level of theory, followed by single-point
197 energy calculations at the M06-2X/ma-TZVP level of theory. On the basis of the
198 calculated Gibbs free energies, the Boltzmann populations (w_i) of each RO₂

199 conformer is expressed as eqn 1.

$$200 \quad w_i = \frac{e^{-\Delta G_i/k_B T}}{\sum_i e^{-\Delta G_i/k_B T}} \quad (1)$$

201 where ΔG_i is the relative Gibbs free energy of conformer i , k_B is the Boltzmann's
202 constant, T is temperature in Kelvin. All the quantum chemical calculations are
203 performed by using the Gaussian 09 program package (Frisch, et al., 2009).

204 **2.2 Kinetics calculations**

205 The rate coefficients of unimolecular reactions are calculated by using the
206 Rice-Ramsperger-Kassel-Marcus theory coupled with energy-grained master equation
207 (RRKM-ME) method (Holbrook, 1996), and the rate coefficients of bimolecular
208 reactions are determined by utilizing traditional transition state theory (TST)
209 (Fernández-Ramos, 2007). The RRKM-ME calculations are performed by
210 implementing the MESMER 6.0 program suite (Glowacki, et al., 2012). N_2 is used as
211 the buffer gas. The single exponential down model is employed to simulate the
212 collision energy transfer ($\langle \Delta E \rangle_{\text{down}} = 200 \text{ cm}^{-1}$). The collisional Lennard-Jones
213 parameters are estimated by using an empirical formula described by Gilbert and
214 Smith (1990). For the H-shift reactions of RO_2 radicals, the rate coefficients are
215 determined by employing the multiconformer transition state theory (MC-TST)
216 approach (Møller, et al., 2016). The MC-TST rate coefficient $k_{\text{MC-TST}}$ is calculated by
217 the sum of the individual intrinsic reaction coordinate TST (IRC-TST) rate coefficient
218 $k_{\text{IRC-TST}}$, each weighted by Boltzmann population of corresponding RO_2 conformer
219 (Møller, et al., 2016).

$$220 \quad k_{\text{MC-TST}} = \sum_i^{\text{all TS conf.}} w_i \times k_{\text{IRC-TST}i} \quad (2)$$

221 where $k_{\text{IRC-TST}i}$ represents the rate coefficient of conformer i , and w_i is the relative
222 Boltzmann population of the corresponding reactant connected to TS_i . The
223 one-dimensional asymmetry Eckart model is employed to calculate the tunneling
224 correction (Eckart, 1930). Considering the uncertainty in barrier heights (~ 1.0
225 kcal mol^{-1} by the M06-2X method) and in tunneling corrections, the uncertainty of the

249 and $-O_2O_3H_2$ groups (R4). For each pathway, a pre-reactive complex with a six- or
250 seven-membered ring structure is formed in the entrance channel, which is stabilized
251 by hydrogen bond interactions between the oxygen atom of OH radical and the
252 abstraction hydrogen atom of HOCH₂OOH, and the remnant hydrogen atom of OH
253 radical and one of oxygen atoms of HOCH₂OOH (Figure S6). Then, it surmounts
254 modest barrier that is higher in energy than the reactants to reaction. The reaction
255 barriers ΔG_a^\ddagger are reduced in the order of 6.4 (R1) > 5.8 (R2) \approx 5.4 (R3) > 1.5 (R4)
256 kcal mol⁻¹, indicating that H-abstraction from the $-O_2O_3H_2$ group (R4) is more
257 preferable than those from the $-O_1H_1$, $-C_1H_3$ and $-C_1H_4$ groups (R1-R3). The same
258 conclusion is also derived from the energy barriers ΔE_a^\ddagger that R4 is the most favorable
259 H-abstraction pathway (Figure S1). The difference of barrier heights can be attributed
260 to the bond dissociation energy (BDE) of different types of bonds in HOCH₂OOH
261 molecule. The BDE decrease in the order of 103.7 (O_1-H_1) > 98.2 (C_1-H_3) \approx 97.4
262 (C_1-H_4) > 87.2 (O_3-H_2) kcal mol⁻¹, which are in good agreement with the order of
263 barrier heights of H-abstraction reactions. As indicated by their reaction free energy
264 values, it can be found that the exothermicity of R4 is the largest among these four
265 H-abstraction reactions. Based on the above discussions, it is concluded that
266 H-abstraction from the $-O_2O_3H_2$ group resulting in formation of HOCH₂OO radical
267 (R4) is feasible on both thermodynamically and kinetically.

268 Considering the different reaction sites of hydrogen atoms, the atmospheric
269 transformation of HOCH(CH₃)OOH from the *anti*-CH₃CHOO + H₂O reaction should
270 have six possible H-abstraction pathways as presented in Figure 3. As shown in
271 Figure 3, each H-abstraction reaction begins with the formation of a weakly bound
272 hydrogen bonded pre-reactive complex with a six- or seven-membered ring structure
273 in the entrance channel (Figure S7). Then it immediately transforms into the
274 respective product via the corresponding transition state. The ΔG_a^\ddagger of H-abstraction
275 from the $-C_1H_3$ (R6) and $-O_2O_3H_2$ (R8) groups are 2.2 and 1.7 kcal mol⁻¹, respectively,
276 which are \sim 4-5 kcal mol⁻¹ lower than those from the $-O_1H_1$ (R5) and $-CH_3$ groups
277 (R7). This result shows that R6 and R8 have nearly identical importance in the
278 atmosphere. Compared with the barriers of H-abstraction at the C_α (R6) and C_β (R7)

279 positions, it can be found that the former case is more favourable than the latter case.
280 This conclusion is further supported by Jara-Toro's study for the reactions of OH
281 radical with linear saturated alcohols (methanol, ethanol and n-propanol) that
282 H-abstraction at the C_α position is predominant (Jara-Toro, et al., 2017, 2018).

283 For the OH-initiated oxidation of HOCH(CH₃)OOH from the *syn*-CH₃CHOO +
284 H₂O reaction, the corresponding free-energy and electronic-energy PESs are
285 displayed in Figures S4 and S5, respectively. From Figure S4, it can be seen the
286 H-abstraction by OH radical from HOCH(CH₃)OOH has six possible pathways. For
287 each pathway, a pre-reactive complex is formed prior to the corresponding transition
288 state, and then it overcomes modest barrier to reaction. The ΔG_a^\ddagger of R6' and R8' are
289 2.3 and 1.8 kcal mol⁻¹, respectively, which are about 5 kcal mol⁻¹ lower than those of
290 R5' and R7'. This result shows that H-abstraction from the -CH (R6') and -OOH (R8')
291 groups are preferable kinetically. The same conclusion is also derived from the energy
292 barriers ΔE_a^\ddagger that the R6' and R8' are the most favourable H-abstraction pathways
293 (Figure S5). It should be noted that although the barriers of R6' and R8' are
294 comparable, the exoergicity of the former case is significantly lower than that of the
295 latter case. The above-mentioned conclusions are consistent with the results derived
296 from the OH-initiated oxidation of HOCH(CH₃)OOH from the *anti*-CH₃CHOO +
297 H₂O reaction. Zhou et al. has demonstrated that the bimolecular reaction of
298 *syn*-CH₃CHOO with water leading to the formation of HOCH(CH₃)OOH is of less
299 importance in the atmosphere, while the unimolecular decay to OH radical is the
300 major loss process of *syn*-CH₃CHOO (Zhou et al., 2019). Therefore, in the present
301 study, we mainly focus on the subsequent mechanism of intermediate generated from
302 OH-initiated oxidation of HOCH(CH₃)OOH from the *anti*-CH₃CHOO + H₂O
303 reaction.

304 From Figure 4, it can be seen that H-abstraction from HOC(CH₃)₂OOH
305 includes eight possible H-abstraction pathways. All the H-abstraction reactions are
306 strongly exothermic and spontaneous, signifying that they are thermodynamically
307 feasible under atmospheric conditions. It deserves mentioning that the release of
308 energy of R12 is significantly greater than those of R9-R11. For each H-abstraction

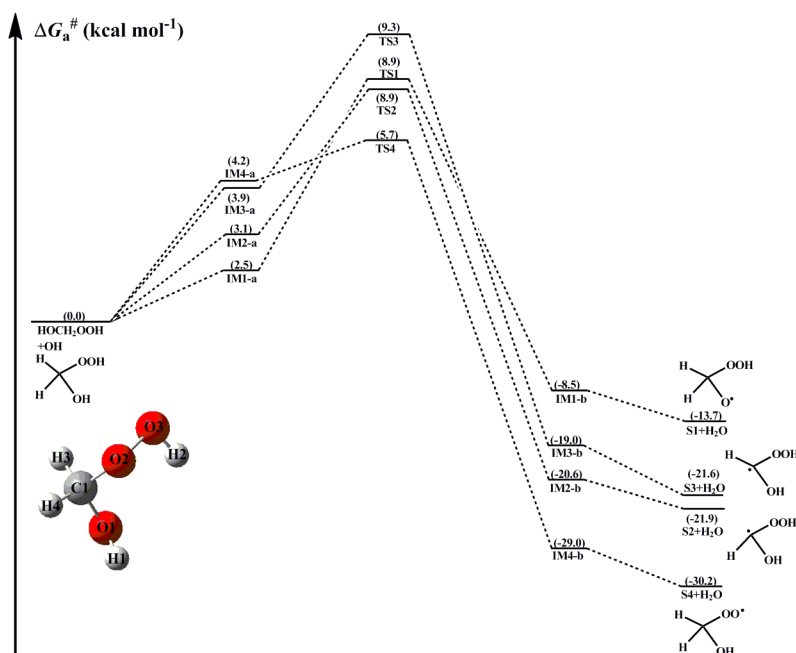
309 pathway, a RC with a six- or seven-membered ring structure is formed prior to the
310 corresponding TS, which is more stable than the separate reactants due to the
311 hydrogen bond interactions between $\text{HOC}(\text{CH}_3)_2\text{OOH}$ and OH radical. Then, the RC
312 overcomes modest barrier to reaction. The ΔG_a^\ddagger of H-abstraction from the $-\text{O}_2\text{O}_3\text{H}_2$
313 group (R12) is $2.7 \text{ kcal mol}^{-1}$, which is the lowest among these eight H-abstraction
314 reactions. This result again shows that the H-abstraction from the $-\text{O}_2\text{O}_3\text{H}_2$ group is
315 the dominant pathway.

316 The rate coefficients of every H-abstraction pathway involved in the initiation
317 reactions of distinct HHPs with OH radical are estimated over the temperature range
318 from 273 to 400 K as summarized in Table S2-S4 and Figures S9-S11. As shown in
319 Table S2, the total rate coefficients k_{tot} of HOCH_2OOH reaction with OH radical
320 decrease slightly with increasing temperature. At ambient temperature, k_{tot} is
321 estimated to be $3.3 \times 10^{-11} \text{ cm}^3 \text{ molecule}^{-1} \text{ s}^{-1}$, which is a factor of ~ 5 greater than the
322 Allen's result ($(7.1 \pm 1.5) \times 10^{-12} \text{ cm}^3 \text{ molecule}^{-1} \text{ s}^{-1}$, at 295 K) derived from the
323 reaction of HMHP with OH radical by using the CF_3O^- chemical ionization mass
324 spectrometry (CIMS) and laser-induced fluorescence (LIF) (Allen, et al., 2018). Such
325 a discrepancy could be attributed to the uncertainty in barrier height and tunneling
326 correction. $k_{\text{R4}(\text{O3-H2})}$ is 1-2 orders of magnitude greater than $k_{\text{R1}(\text{O1-H1})}$, $k_{\text{R2}(\text{C1-H3})}$ and
327 $k_{\text{R3}(\text{C1-H4})}$ in the whole temperature range, implying that R4 is the most favorable
328 H-abstraction pathway. For example, $k_{\text{R4}(\text{O3-H2})}$ is calculated to be $2.9 \times 10^{-11} \text{ cm}^3$
329 $\text{molecule}^{-1} \text{ s}^{-1}$ at 298 K, which is higher than $k_{\text{R1}(\text{O1-H1})}$ (1.8×10^{-13}), $k_{\text{R2}(\text{C1-H3})}$ ($9.9 \times$
330 10^{-13}) and $k_{\text{R3}(\text{C1-H4})}$ (2.0×10^{-12}) by 161, 29 and 15 times, respectively.

331 From Table S3, it can be seen that the total rate coefficients k'_{tot} of
332 $\text{HOCH}(\text{CH}_3)\text{OOH}$ reaction with OH radical decrease in the range of 4.5×10^{-11} (273
333 K) to 8.1×10^{-12} (400 K) $\text{cm}^3 \text{ molecule}^{-1} \text{ s}^{-1}$ with increasing temperature, and they
334 exhibit a slightly negative temperature dependence. $k_{\text{R8}(\text{O3-H2})}$ are approximately
335 identical to k'_{tot} in the entire temperature range, which are 1-2 orders of magnitude
336 greater than $k_{\text{R5}(\text{O1-H1})}$, $k_{\text{R6}(\text{C1-H3})}$, $k_{\text{R7-1}(\text{C2-H4})}$, $k_{\text{R7-2}(\text{C2-H5})}$ and $k_{\text{R7-3}(\text{C2-H6})}$. The result again
337 shows that H-abstraction from the $-\text{OOH}$ group (R8) is preferable kinetically. It
338 should be noted that although the barriers of R8 and R6 are comparable, $k_{\text{R8}(\text{O3-H2})}$ is

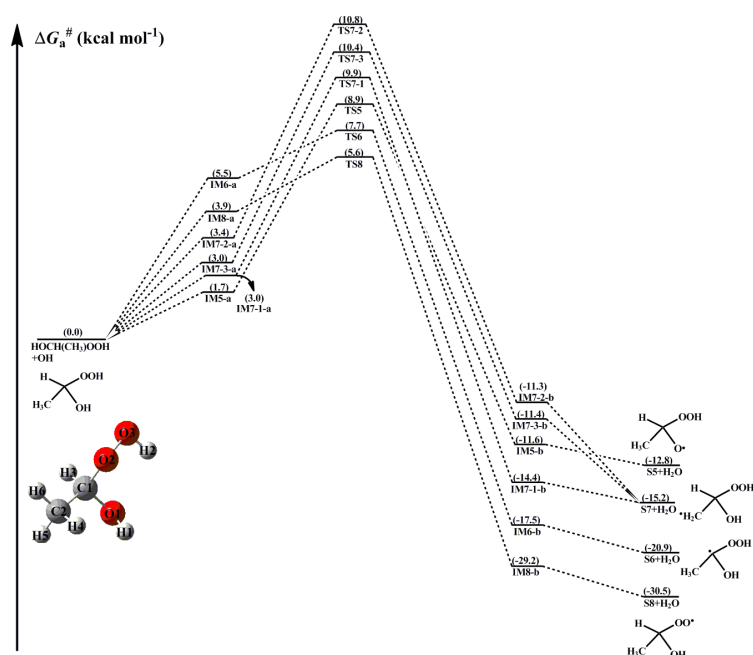
339 about one order of magnitude higher than $k_{R6(C1-H3)}$ over the temperature range studied.
340 The most likely reason is due to the stability of pre-reactive complexes that IM8-a is
341 more stable than IM6-a in energy. A similar conclusion is derived from the results of
342 rate coefficients of $\text{HOC}(\text{CH}_3)_2\text{OOH} + \text{OH}$ reaction that H-abstraction from the -OOH
343 group (R12) is favorable kinetically (Table S4). The atmospheric lifetime of
344 HOCH_2OOH , $\text{HOCH}(\text{CH}_3)\text{OOH}$ and $\text{HOC}(\text{CH}_3)_2\text{OOH}$ reactivity toward OH radical
345 are estimated to be 0.58-1.74 h, 0.60-1.79 h and 1.23-3.69 h at room temperature
346 under typical OH radical concentrations of $5\text{-}15 \times 10^6$ molecules cm^{-3} during daylight
347 (Long et al., 2017).

348 In summary, the dominant pathway is the H-abstraction from the -OOH group in
349 the initiation reactions of OH radical with HOCH_2OOH . H-abstraction from the -CH
350 group is competitive with that from the -OOH group in the reaction of OH radical
351 with $\text{HOCH}(\text{CH}_3)\text{OOH}$. Compared with the barriers of H-abstraction from the -OOH
352 and -CH₂ groups in the reaction of OH radical with HOCH_2OOH , it can be found
353 that the barrier of H-abstraction from the -CH group is reduced by $3.6 \text{ kcal mol}^{-1}$,
354 whereas the barrier of H-abstraction from the -OOH group is increased by 0.2
355 kcal mol^{-1} when a methyl group substitution occurs at the C1-position of
356 HOCH_2OOH . The dominant pathway is the H-abstraction from the -OOH group in
357 the reaction of OH radical with $\text{HOC}(\text{CH}_3)_2\text{OOH}$, and the barrier height is increased
358 by $1.2 \text{ kcal mol}^{-1}$ compared to the OH + HOCH_2OOH system. The barrier of
359 H-abstraction from the -OOH group is slightly increased as the number of methyl
360 group is increased. It is interesting to compare the rate coefficient of dominant
361 pathway in the OH + HOCH_2OOH system with that for the analogous reactions in
362 the OH + $\text{HOCH}(\text{CH}_3)\text{OOH}$ and OH + $\text{HOC}(\text{CH}_3)_2\text{OOH}$ reactions. It can be found
363 that the rate coefficient is almost identical when a methyl group substitution occurs
364 at the C₁-position, whereas the rate coefficient reduces by a factor of 2-5 when two
365 methyl groups are introduced into the C₁-position.



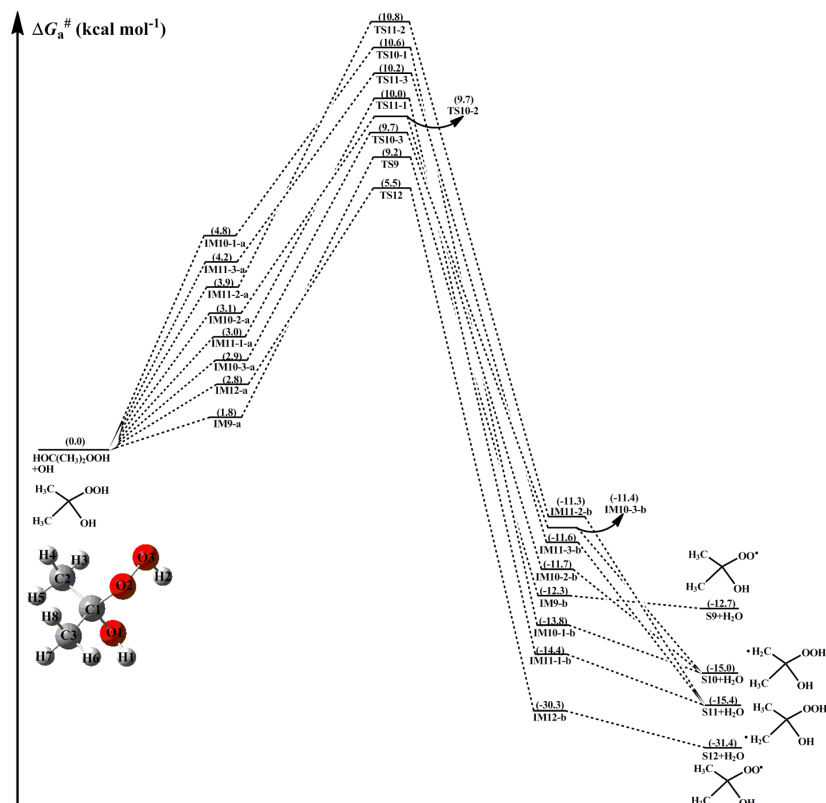
366

367 **Figure 2.** PES (ΔG_a^\ddagger) for the OH-initiated reactions of HOCH₂OOH from the CH₂OO + H₂O
 368 reaction predicted at the M06-2X/ma-TZVP//M06-2X/6-311+G(2df,2p) level of theory (a and b
 369 represent the pre-reactive and post-reactive complexes)



370

371 **Figure 3.** PES (ΔG_a^\ddagger) for the OH-initiated reactions of HOCH(CH₃)OOH from the
 372 *anti*-CH₃CHOO + H₂O reaction predicted at the M06-2X/ma-TZVP//M06-2X/6-311+G(2df,2p)
 373 level of theory (a and b represent the pre-reactive and post-reactive complexes)



374

375 **Figure 4.** PES (ΔG_a^\ddagger) for the OH-initiated reactions of HOC(CH₃)₂OOH from the (CH₃)₂COO +
 376 H₂O reaction predicted at the M06-2X/ma-TZVP//M06-2X/6-311+G(2df,2p) level of theory (a
 377 and b represent the pre-reactive and post-reactive complexes)

378 3.2 Subsequent reactions of H-abstraction products RO₂ radicals 379 in pristine environments

380 In principle, the H-abstraction products RO₂ radicals have three possible fates in
 381 pristine environments: (1) the self-reactions of RO₂ radicals can either produce RO +
 382 R'O + O₂ (propagation channel), or generate ROH + R'(-H, =O) + O₂ or produce
 383 ROOR + O₂ (termination channel) that has been recognized as an important SOA
 384 precursor (Berndt et al., 2018; Zhang et al., 2012); (2) RO₂ radicals react with HO₂
 385 radical leading to the formation of hydroperoxide ROOH, alcohol, OH and other
 386 products (Winiberg et al., 2016; Chen et al., 2021); (3) RO₂ radicals autoxidation
 387 through intramolecular H-shift and alternating O₂ addition steps generate HOMs (Ehn
 388 et al., 2014; Bianchi et al., 2019; Nozière and Vereecken, 2019; Rissanen et al., 2014).
 389 The relevant details for these three kinds of reactions will be discussed in the
 390 following paragraph.

391 **3.2.1 Reactions mechanism for the self-reaction of RO₂ radicals**

392 The self-reaction is one of dominant removal pathways for RO₂ radicals when
393 the concentration of NO is low and the concentration of RO₂ radicals is high. The
394 self-reaction of RO₂ radicals usually follows the Russell mechanism (Russell, 1957),
395 and mainly includes four possible pathways: (1) $2\text{RO}_2 \rightarrow 2\text{RO} + \text{O}_2$; (2) $2\text{RO}_2 \rightarrow$
396 $\text{ROH} + \text{R}'\text{CO} + \text{O}_2$; (3) $2\text{RO}_2 \rightarrow \text{ROOR} + \text{O}_2$; (4) $2\text{RO}_2 \rightarrow \text{ROOH} + \text{R}'\text{CHOO}$
397 (Atkinson and Arey, 2003). The relative importance of different pathways is varied
398 considerably depending on the nature of RO₂ radicals (Valiev et al., 2019; Lee et al.,
399 2016). A schematic PES for the self-reaction of HOCH₂OO radical is drawn in Figure
400 5. As can be seen in Figure 5a, the self-reaction of HOCH₂OO radical starts with the
401 formations of tetroxide complexes IM13-a and IM14-a in the entrance channel, with
402 2.9 and 3.4 kcal mol⁻¹ stability. Then they fragment into dimer S13 + ¹O₂ (R13) and
403 HOCH₂OOH + HOCHOO (R14) via transition states TS13 and TS14 with the barriers
404 of 43.3 and 51.5 kcal mol⁻¹. But the barriers of R13 and R14 are extremely high,
405 making them irrelevant in the atmosphere.

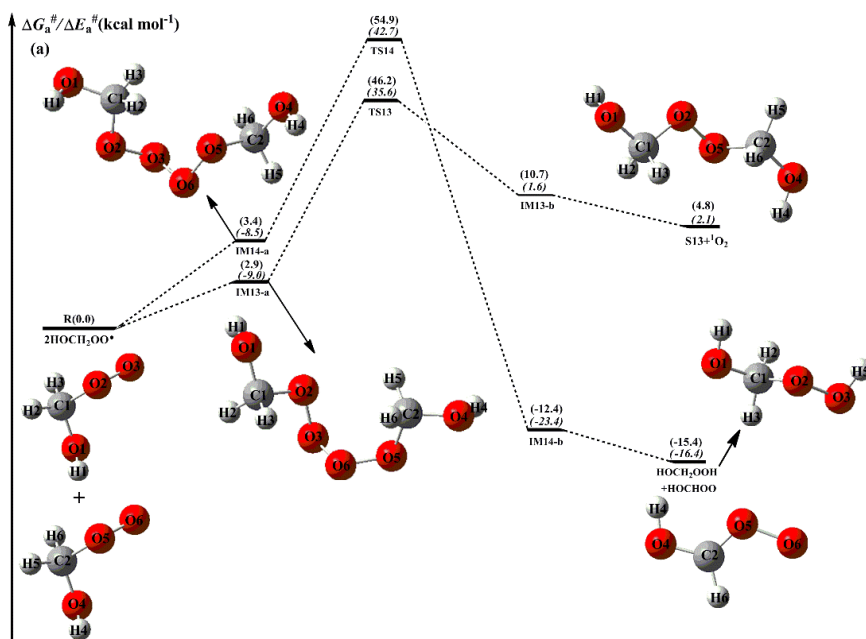
406 From Figure 5b, it is seen that the self-reaction of HOCH₂OO radical proceeds
407 via oxygen-to-oxygen coupling leading to the formation of tetroxide intermediate S14
408 with the electronic energy and free energy barriers of 7.3 and 19.6 kcal mol⁻¹. Kumar
409 and Francisco reported that the electronic energy barrier of the gas phase
410 decomposition of HOCH₂OO radical is 14.0 kcal mol⁻¹ and it could be a new source
411 of HO₂ radical in the troposphere (Kumar and Francisco, 2015, 2016). Compared with
412 the electronic energy barriers of unimolecular dissociation of HOCH₂OO radical and
413 its self-reaction, it can be found that the self-reaction of HOCH₂OO radical resulting
414 in formation of S14 is significantly feasible. The formed S14 can fragment into
415 HOCH₂O + HCOOH + HO₂ via a concerted process of O₂-O₃ and O₅-O₆ bonds
416 rupture and O₃-H₆ bond forming with the barrier of 29.8 kcal mol⁻¹. Alternatively, S14
417 can convert into the caged tetroxide intermediate S16 through the asymmetric two
418 step O₂-O₃ and O₅-O₆ bonds scission with the barriers of 19.1 and 3.1 kcal mol⁻¹,
419 respectively. The result shows that the latter pathway is more preferable than the

420 former channel owing to its lower barrier. The overall spin multiplicity of S16 is
421 singlet, in which the O₂ moiety maintains the triplet ground state (spin up) and is very
422 loosely bound. In order to preserve the overall singlet multiplicity, the two HOCH₂O
423 radical pairs (³(HOCH₂O ··HOCH₂O)) must have the triplet multiplicity (spin down).
424 S16 could be regarded as the ground state ³O₂ moving away from the two HOCH₂O
425 radical pairs that keep interacting. Due to the difficulty in performing the constrained
426 optimization for the dissociation of S16, the ³O₂ moiety is considered as a leaving
427 moiety away from two HOCH₂O radical pairs, and merely the dissociation of
428 ³(HOCH₂O ··HOCH₂O) is taken into consideration in the present study. It has three
429 types of pathways: (1) it yields HOCH₂OH and excited-state ³HCOOH through the
430 alpha hydrogen transfer with the barrier of 14.0 kcal mol⁻¹ and 10.2 kcal mol⁻¹
431 exothermicity, followed by the excited ³HCOOH to go back to the ground-state
432 ¹HCOOH; (2) it generates two HOCH₂O radicals via the barrierless process with the
433 exoergicity of 16.9 kcal mol⁻¹; (3) it produces dimer S17 via an intersystem crossing
434 (ISC) step with the exoergicity of 32.1 kcal mol⁻¹. Based on the calculated reaction
435 barriers, it can be found that the rate-limiting step is the cleavage of O₂-O₃ bond (R17)
436 in the unimolecular decay processes of S14. This conclusion coincides with the
437 previous result obtained from the dissociation of di-t-butyl tetroxide that the
438 rate-controlling step is the rupture of single O-O bond (Lee et al., 2016). Valiev et al.
439 (2019) proposed that the ISC rate of ROOR dimer formed from the different
440 (RO ··R'O) systems is extremely rapid (> 10⁸ s⁻¹) and exhibits a strong
441 stereoselectivity.

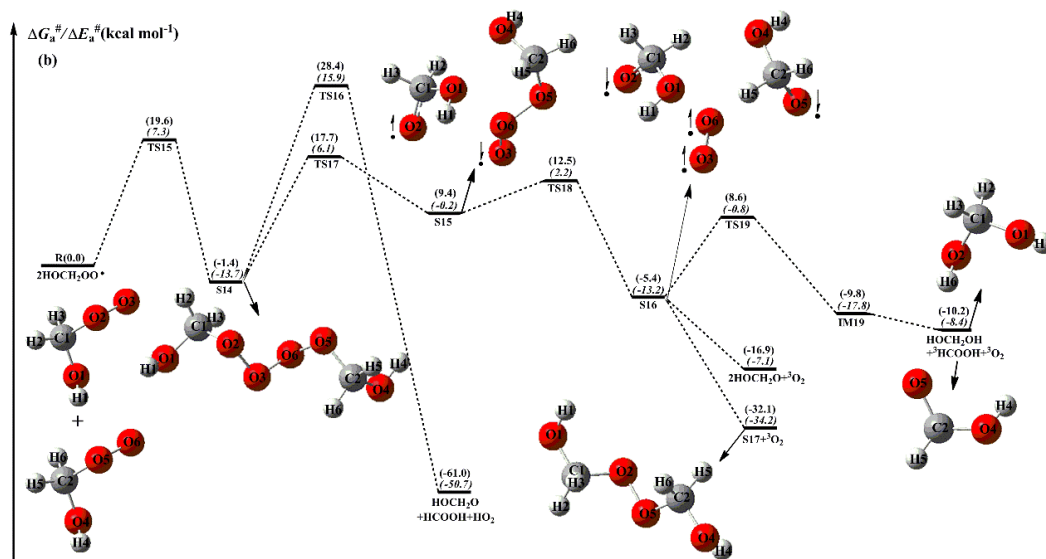
442 Figure 6 depicts a schematic PES for the self-reaction of HOCH(CH₃)OO radical.
443 As shown in Figure 6a, the self-reaction of HOCH(CH₃)OO radical can either
444 produce dimer S18 along with ¹O₂ via transition state TS20 with the barrier of 44.4
445 kcal mol⁻¹, or generate HOCH(CH₃)OOH and HOC(CH₃)OO through transition state
446 TS21 with the barrier of 54.3 kcal mol⁻¹. But the barriers of R20 and R21 are
447 significantly high, making them of less importance in the atmosphere. Alternatively,
448 the self-reaction of HOCH(CH₃)OO radical proceeds via an oxygen-to-oxygen
449 coupling resulting in formation of tetroxide intermediate S19 with the barrier of 19.9

450 kcal mol⁻¹ (Figure 6b). The formed S19 proceeds through the asymmetric two step
451 O₂-O₃ and O₅-O₆ bonds scission to produce a caged tetroxide intermediate S21 of
452 overall singlet multiplicity comprising two same-spin alkoxy radicals (spin down)
453 and triplet oxygen (spin up). These two processes overcome the barriers of 21.4 and
454 1.3 kcal mol⁻¹, respectively. Then, S21 decomposes into the propagation
455 (2HOCH(CH₃)O + ³O₂) and termination products (HOCH(CH₃)OH + ³CH₃OOH +
456 ³O₂ and dimer S22 + ³O₂) with the exoergicity of 12.5, 11.7 and 33.0 kcal mol⁻¹. The
457 rate-determining step is the rupture of O₂-O₃ bond (R24) in the dissociation processes
458 of S19.

459 As shown in Figure 7, the dominant pathway for the self-reaction of
460 HO(CH₃)₂COO radical begins with the formation of tetroxide intermediate S24 via an
461 oxygen-to-oxygen coupling transition state TS28 with the barrier of 20.4 kcal mol⁻¹;
462 then it transforms into the caged tetroxide intermediate S26 of overall singlet spin
463 multiplicity through the asymmetric two-step O-O bond cleavage with the barriers of
464 22.0 and 3.4 kcal mol⁻¹; finally, S26 can either produce two HO(CH₃)₂CO radicals
465 with the exoergicity of 10.3 kcal mol⁻¹, or generate dimer S27 with the exothermicity
466 of 31.5 kcal mol⁻¹. Compared with the self-reactions of HOCH₂OO and
467 HOCH(CH₃)OO radicals, it can be found that the termination product of the
468 self-reaction of HOC(CH₃)₂OO radical is exclusively dimer S27. The reason is due to
469 the absence of alpha hydrogen atom in HOC(CH₃)₂OO radical. Compared with the
470 barrier of rate-determining route R17 in the self-reaction of HOCH₂OO radical, it can
471 be found that the barrier of rate-limiting step R29 is increased by about 3.0 kcal mol⁻¹
472 when two methyl substitutions are introduced into the C1-position of HOCH₂OO
473 radical. The reason might be attributed to the cage escape of alkoxy radicals. It is
474 therefore that the tertiary RO₂ radicals have great opportunity to react with HO₂
475 radical or undergo autoxidation in pristine environments.



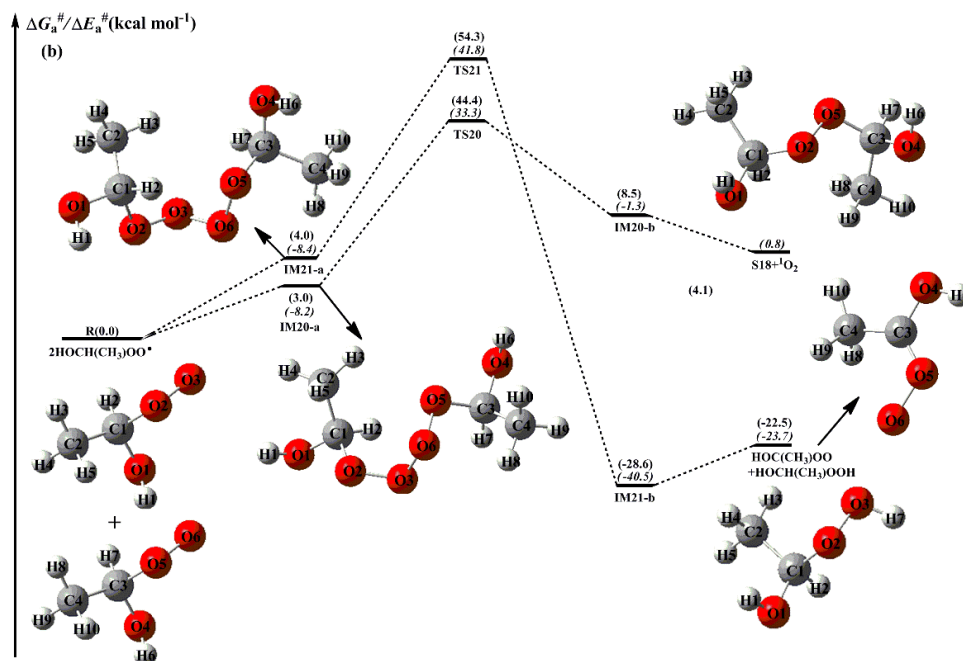
476



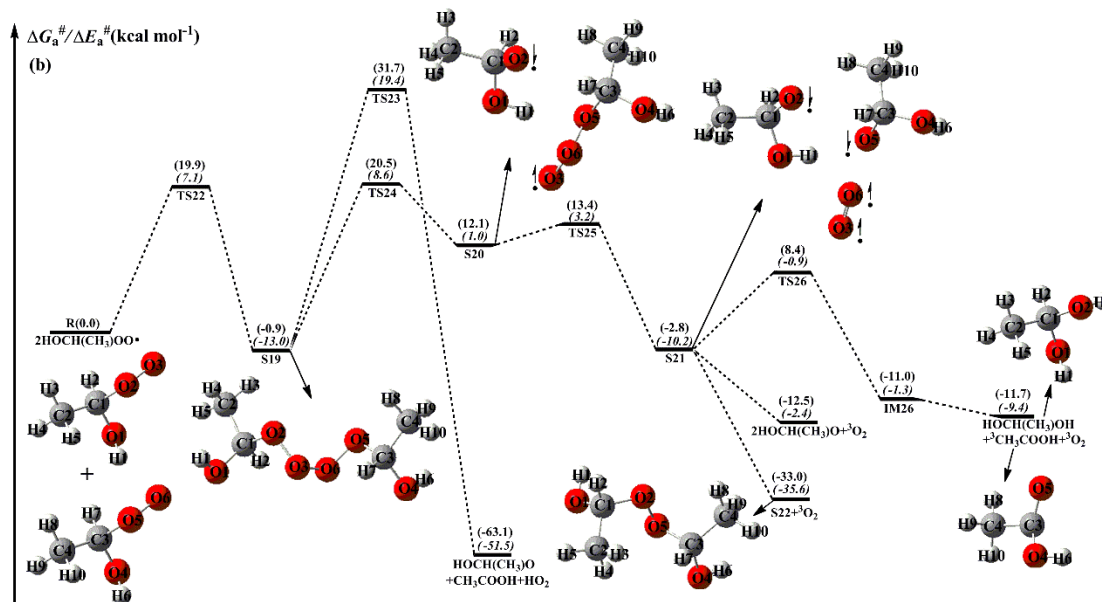
477

478 **Figure 5.** PES (ΔG_a^\ddagger and ΔE_a^\ddagger , in italics) for the self-reaction of HOCH₂OO predicted at
 479 the M06-2X/ma-TZVP//M06-2X/6-311+G(2df,2p) level of theory

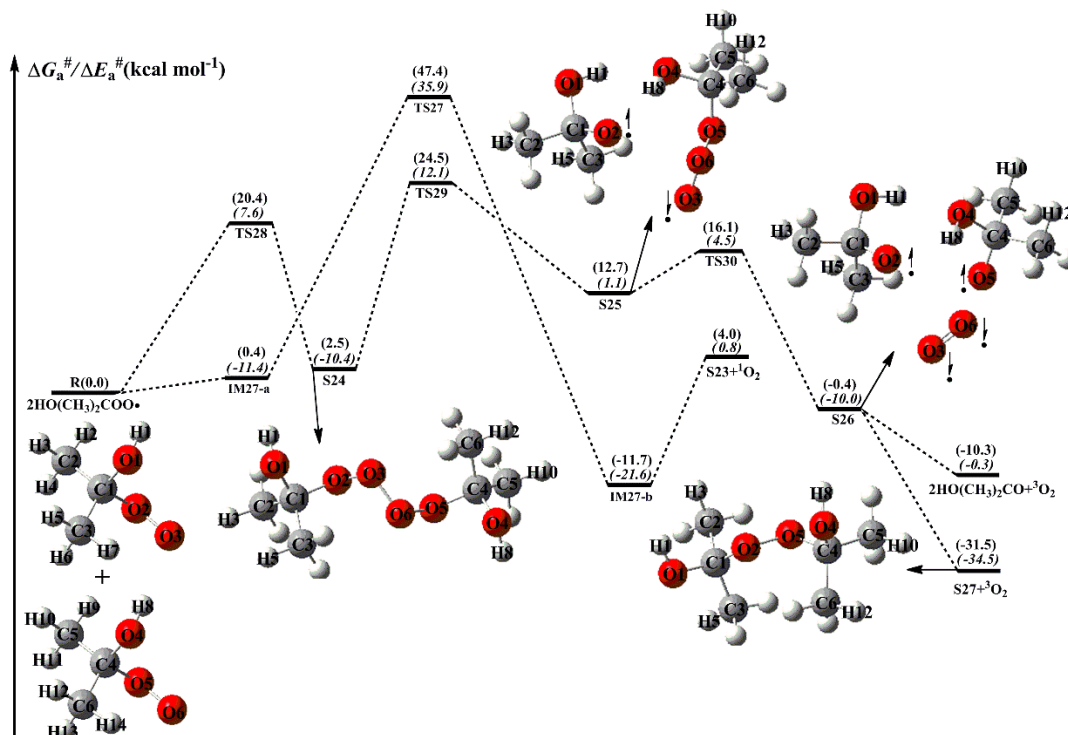
480



481



482 **Figure 6.** PES ($\Delta G_a^\#$ and $\Delta E_a^\#$, in italics) for the self-reaction of HOCH(CH₃)OO radicals
 483 predicted at the M06-2X/ma-TZVP//M06-2X/6-311+G(2df,2p) level of theory



484

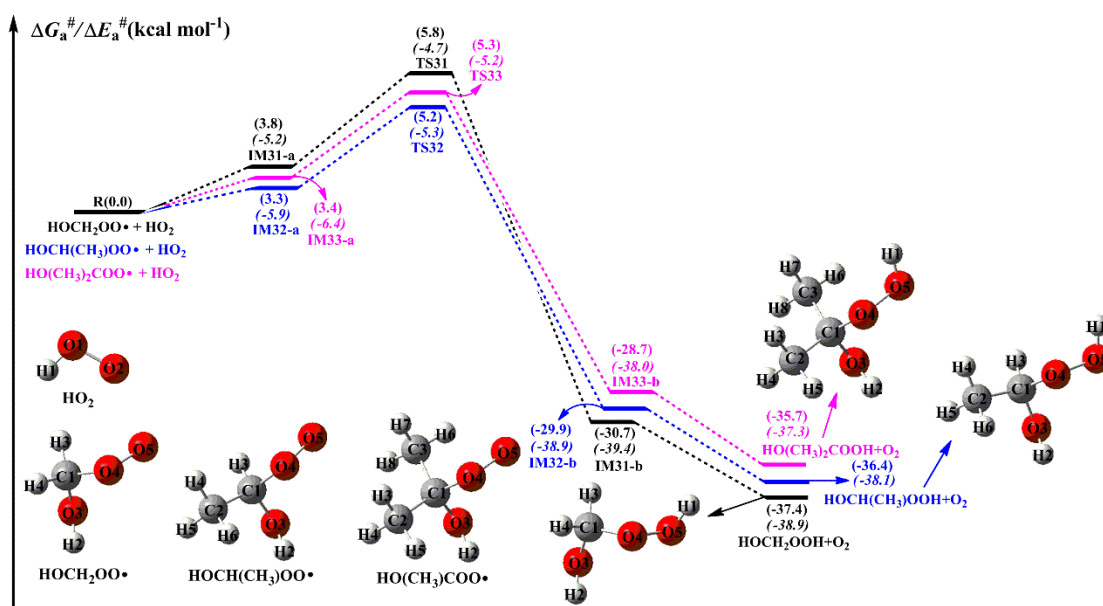
485 **Figure 7.** PES (ΔG_a^\ddagger and ΔE_a^\ddagger , in italics) for the self-reaction of $\text{HO}(\text{CH}_2)_2\text{COO}$ radicals
 486 predicted at the M06-2X/ma-TZVP//M06-2X/6-311+G(2df,2p) level of theory

487 **3.2.2 Reactions mechanism for the reaction of RO_2 radicals with HO_2**
 488 **radical**

489 When NO is present in low concentration, the bimolecular reaction of RO_2
 490 radicals with HO_2 radical is generally expected to be the dominant pathway as the
 491 main product hydroperoxide ROOH . The primary sources of HO_2 radical involve the
 492 photo-oxidation of oxygenated volatile organic compounds (OVOCs) and the
 493 ozonolysis reaction, as well as secondary sources include the reactions of OH radical
 494 with CO, ozone and volatile organic compounds (VOCs), the reaction of alkoxy
 495 radical RO with O_2 and the red-light-induced decomposition of α -hydroxy
 496 methylperoxy radical OHCH_2OO (Kumar and Francisco, 2015; Stone et al., 2012;
 497 Hofzumahaus et al., 2009). The atmospheric concentration of HO_2 radical is $1.5\text{-}10 \times$
 498 10^8 molecules cm^{-3} at ground level in polluted urban environments (Stone et al., 2012).
 499 A schematic PES for the reactions of distinct RO_2 radicals with HO_2 radical is
 500 presented in Figure 8. As shown in Figure 8, all the reactions are strongly exothermic
 501 and spontaneous, indicating that they are feasible thermodynamically in the
 502 atmosphere. The reaction for HOCH_2OO with HO_2 (R31) starts with the formation of

503 a pre-reactive complex IM31-a in the entrance channel, which is more stable than the
504 separate reactants by $3.8 \text{ kcal mol}^{-1}$ in energy. Then it converts into HOCH₂OOH and
505 O₂ via a hydrogen atom transfer from the HO₂ radical to the terminal oxygen atom of
506 HOCH₂OO radical with the barrier of $2.0 \text{ kcal mol}^{-1}$. The mechanism of
507 HOCH(CH₃)OO + HO₂ (R32) and HO(CH₃)₂COO + HO₂ (R33) reactions is quite
508 similar to that of HOCH₂OO + HO₂ system. In order to avoid redundancy, we will not
509 discuss them in detail. It deserves mentioning that the barrier height is only reduced
510 by $0.1 \text{ kcal mol}^{-1}$ when one or two methyl substitutions occur at the C1-position of
511 HOCH₂OO radical, compared to the barrier of HOCH₂OO + HO₂ reaction. This result
512 implies that the barrier height is not seem to be influenced by the number of methyl
513 substitution. The rate coefficients of distinct RO₂ radical reactions with HO₂ radical
514 are summarized in Table S5 and Figure S12. As shown in Table S5, the rate
515 coefficients k_{R31} of HOCH₂OO + HO₂ reaction vary from 3.1×10^{-11} (273 K) to $2.1 \times$
516 $10^{-12} \text{ cm}^3 \text{ molecule}^{-1} \text{ s}^{-1}$ (400 K), and they exhibit a negative temperature dependence.
517 Similar conclusion is also obtained from the rate coefficients k_{R32} and k_{R33} that they
518 decrease with the temperature increasing. It should be noted that the rate coefficient is
519 slightly increased as the number of methyl group is increased. At ambient temperature,
520 k_{R31} is estimated to be $1.7 \times 10^{-11} \text{ cm}^3 \text{ molecule}^{-1} \text{ s}^{-1}$, which is in good agreement with
521 the value of $\sim 2 \times 10^{-11} \text{ cm}^3 \text{ molecule}^{-1} \text{ s}^{-1}$ for the reaction of acyl peroxy radicals with
522 HO₂ radical (Wennberg et al., 2018). The typical atmospheric concentrations of HO₂
523 radical are 5, 20 and 50 pptv in the urban, rural and forest environments (Bianchi et
524 al., 2019), translating into the pseudo-first-order rate constants $k'_{HO_2} = k_{HO_2}[HO_2]$ of
525 1.1×10^{-3} , 4.2×10^{-3} and $1.1 \times 10^{-2} \text{ s}^{-1}$, respectively. The pseudo-first-order rate
526 constants of R32 and R33 are predicted to be 3.0×10^{-3} and 4.8×10^{-3} (urban), $1.1 \times$
527 10^{-2} and 1.8×10^{-2} (rural), 3.0×10^{-2} and $4.8 \times 10^{-2} \text{ s}^{-1}$ (forest) at room temperature.

528



529

530 **Figure 8.** PES (ΔG_a^\ddagger and ΔE_a^\ddagger , in italics) for the reactions of HO₂ radical with distinct RO₂
 531 radicals predicted at the M06-2X/ma-TZVP//M06-2X/6-311+G(2df,2p) level of theory

532 3.2.3 Reactions mechanism for the isomerization of RO₂ radicals

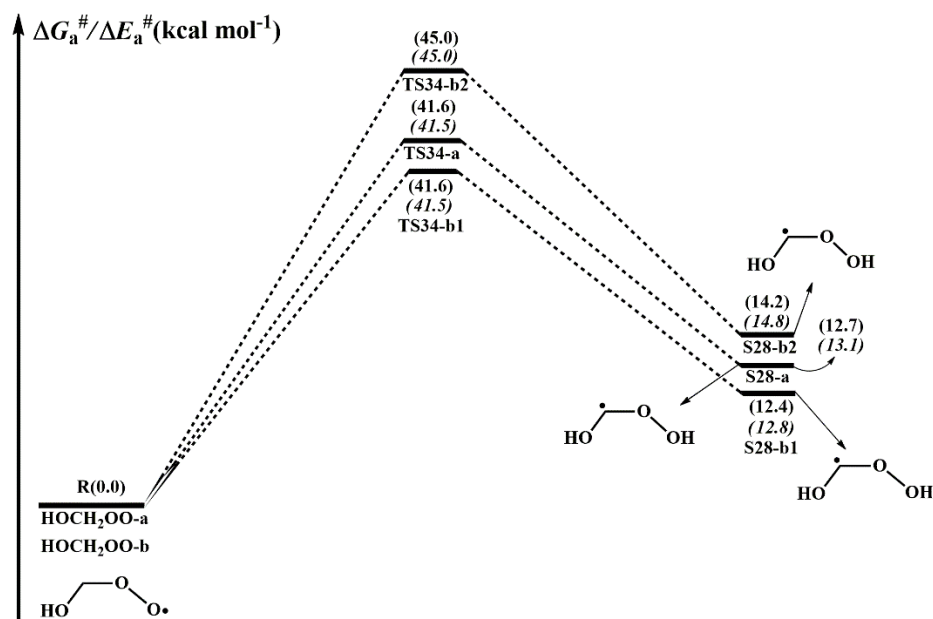
533 Autoxidation of RO₂ radicals is known to play an important role in the
 534 (re)generation of HO_x radicals and in the formation of HOMs (Xu et al., 2014;
 535 Bianchi et al., 2019; Rissanen et al., 2014; Ehn et al., 2017). The autoxidation
 536 mechanism includes an intramolecular H-shift from the -CH₃ or -CH₂- groups to the
 537 -OO site, leading to the formation of a hydroperoxyalkyl radical QOOH, followed by
 538 O₂ addition to form a new peroxy radical (HOOQO₂), one after the other, resulting in
 539 formation of HOMs (Rissanen et al., 2014; Berndt et al., 2015). For the H-shift
 540 reactions of RO₂ radicals, reactants, transition states and products have multiple
 541 conformers due to the effect of degree of freedom for internal rotation. Based on the
 542 calculated results, it can be found that HOCH₂OO radical has four energetically
 543 similar conformers (HOCH₂OO-a, HOCH₂OO-b, HOCH₂OO-c and HOCH₂OO-d).
 544 The relative free energy and Boltzmann population (w_i) of individual conformer are
 545 listed in Table S6. As shown in Table S6, the Boltzmann populations of these four
 546 conformers are 46.39, 46.31, 2.99 and 4.32%, respectively.

547 A schematic PES for the H-shift reaction of HOCH₂OO radical is displayed in
 548 Figure 9. As can be seen in Figure 9, the lowest-energy conformer HOCH₂OO-a can
 549 proceed via a 1,3-H shift from the -CH₂ group to the terminal oxygen leading to the

550 formation of S28-a (HOCHOOH) with the barrier of 41.6 kcal mol⁻¹. HOCH₂OO-b
551 can isomerize to S28-b1 and S28-b2 via the four-membered ring transition states
552 TS34-b1 and TS34-b2 (1,3-H shifts) with the barriers of 41.6 and 45.0 kcal mol⁻¹. But
553 these three 1,3-H shift reactions have comparatively high barriers, making them
554 irrelevant in the atmosphere. Despite many attempts, the transition states of H-shift
555 reactions of HOCH₂OO-c and HOCH₂OO-d are not located. The result implies that
556 the H-shift reactions of these two conformers are inhibited, which is consistent with
557 the previous study that not all reactants will be in a conformation with a path across
558 the barrier to reaction in the H-shift reactions of RO₂ radicals (Møller et al., 2016).
559 Equivalent to the case of HOCH₂OO radical, the isomerization of HOCH(CH₃)OO
560 radical proceeds via the 1,3- and 1,4-H shifts from the -CH or -CH₃ groups to the
561 terminal oxygen resulting in formation of hydroperoxyalkyl radicals (Figure S13).
562 These 1,3- and 1,4-H shift reactions accompany with the extremely high barriers (>
563 37.9 kcal mol⁻¹), implying that they are of less importance in the atmosphere. Similar
564 conclusion is also derived from the isomerization of HO(CH₃)₂COO radical that 1,4-H
565 shift reactions are unfavourable kinetically (Figure S14). The high barriers of 1,3- and
566 1,4-H shifts can be interpreted as the result of the large ring strain energy (RSE) in the
567 cyclic transition state geometries. As a consequence, the isomerization reactions of
568 HOCH₂OO, HOCH(CH₃)OO and HO(CH₃)₂COO radicals are unlikely to proceed in
569 the atmosphere. This conclusion is further supported by the previous studies that the
570 intramolecular H-shift isomerizations are important only for RO₂ radicals with larger
571 carbon structures (Crouse et al., 2013; Jokinen et al., 2014; Rissanen et al., 2014).

572 The single-conformer rate coefficients ($k_{\text{IRC-TST}}$) and multi-conformer rate
573 coefficients ($k_{\text{MC-TST}}$) of the isomerization of HOCH₂OO, HOCH(CH₃)OO and
574 HOC(CH₃)₂OO radicals are calculated over the temperature range of 273-400 K as
575 listed in Table S9-S11. As can be seen in Table S9, $k_{\text{IRC-TST}}$ of each conformer exhibits
576 a marked positive temperature dependence over the temperature range studied.
577 $k_{\text{MC-TST}}$ is significantly increased with rising temperature, implying that the
578 temperature increasing is beneficial to the occurrence of HOCH₂OO radical
579 isomerization. Similar conclusion is also obtained from the isomerization of

580 HOCH(CH₃)OO and HOC(CH₃)₂OO radicals (Table S10-S11). It is worth mentioning
 581 that $k_{\text{MC-TST}}$ is rapidly increased as the number of methyl group is increased. For
 582 example, the room temperature $k_{\text{MC-TST}}$ of HOCH₂OO radical isomerization is
 583 calculated to be $4.4 \times 10^{-16} \text{ s}^{-1}$, which is lower than those of the HOCH(CH₃)OO (2.9
 584 $\times 10^{-13} \text{ s}^{-1}$) and HO(CH₃)₂COO ($3.0 \times 10^{-12} \text{ s}^{-1}$) radicals isomerization by 660 and
 585 6820 times, respectively.



586
 587 **Figure 9.** PES (ΔG_a^\ddagger and ΔE_a^\ddagger , in italics) for the isomerization of HOCH₂OO radical predicted at
 588 the M06-2X/ma-TZVP//M06-2X/6-311+G(2df,2p) level of theory

589 3.3 Subsequent reactions of H-abstraction products RO₂ radicals 590 in urban environments

591 NO_x is present in high concentration in urban environments, reaction with NO is
 592 the dominant chemical sink for RO₂ radicals (Atkinson and Arey, 2003; Orlando and
 593 Tyndall, 2012; Perring et al., 2013). The main pathways in this type of reaction lead to
 594 the formations of NO₂, RO radicals, organic nitrites, and organic nitrates, and their
 595 formation yields are highly dependent on the nature of R group (Orlando and Tyndall,
 596 2012). The formation of NO₂ through subsequent photolysis ($\lambda < 420 \text{ nm}$) produces
 597 ozone and NO, increasing the concentrations of near-surface ozone and propagating
 598 NO_x chain (Orlando and Tyndall, 2012). The schematic PES for the reactions of
 599 distinct RO₂ radicals with NO are displayed in Figures 10-12. As shown in Figure 10,
 600 the bimolecular reaction of HOCH₂OO radical with NO initially leads to nitrite adduct

601 S31 via the barrierless addition of NO to terminal oxygen atom O₃ of HOCH₂OO
602 radical. The formed S31 exists two isomers: S31-*cis* refers to the O₂ and O₄ on the
603 same side ($\text{DO}_2\text{O}_3\text{N}_1\text{O}_4 = 2.3^\circ$), whereas S31-*trans* refers to the O₂ and O₄ on the
604 opposite side ($\text{DO}_2\text{O}_3\text{N}_1\text{O}_4 = -179.8^\circ$) with respect to the O₃-N₁ bond. The
605 calculations show that S31-*cis* is more stable than S31-*trans* by 1.1 kcal mol⁻¹ in
606 energy. The tautomerization between S31-*cis* and S31-*trans* proceeds through the
607 rotating of O₃-N₁ bond with the barrier of 14.4 kcal mol⁻¹, implying that they can be
608 regarded as the separate atmospheric species. According to the Boltzmann-weighted
609 distribution, at room temperature, the predicted percentages of S31-*cis* and S31-*trans*
610 are 86.5% and 13.5%, respectively. The result implies that the dominant product of
611 HOCH₂OO radical reaction with NO is S31-*cis*, and it is selected as a model
612 compound to insight into the mechanism of secondary reactions in the following
613 sections.

614 S31-*cis* can either isomerize to organic nitrate S32 (R38) via a concerted
615 process of O₂-O₃ bond breaking and O₂-N₁ bond forming with the barrier of 47.8
616 kcal mol⁻¹, or decompose into HOCH₂O radical and NO₂ (R39) via the cleavage of
617 O₂-O₃ bond with the barrier of 11.3 kcal mol⁻¹. The result shows that the latter
618 pathway is more favourable than the former channel. Similar conclusion is also
619 obtained from the reactions of NO with HOCH(CH₃)OO and HO(CH₃)₂COO radicals
620 that the formation of organic nitrate is of minor importance in the atmosphere. This
621 result is further supported by the prior studies that the direct formation of organic
622 nitrate from peroxy nitrites is a minor channel in the reactions of isoprene-derived
623 RO₂ radicals with NO (Piletic et al., 2017; Zhang et al., 2002). It should be noted that
624 the transition state TS39 is not located using M06-2X functional, but it is located at
625 the MP2/6-311+G(2df,2p) level of theory and is verified using IRC calculations. The
626 formed HOCH₂O radical has two possible pathways: (1) it directly decomposes into
627 CH₂O and OH radical (R40) via β -site C₁-O₁ bond scission with the barrier of 52.4
628 kcal mol⁻¹; (2) it converts into HCOOH and HO₂ radical (R41) through H-abstraction
629 by O₂ with the barrier of 26.4 kcal mol⁻¹. This result reveals that R41 is the most
630 feasible channel in the fragmentation of HOCH₂O radical.

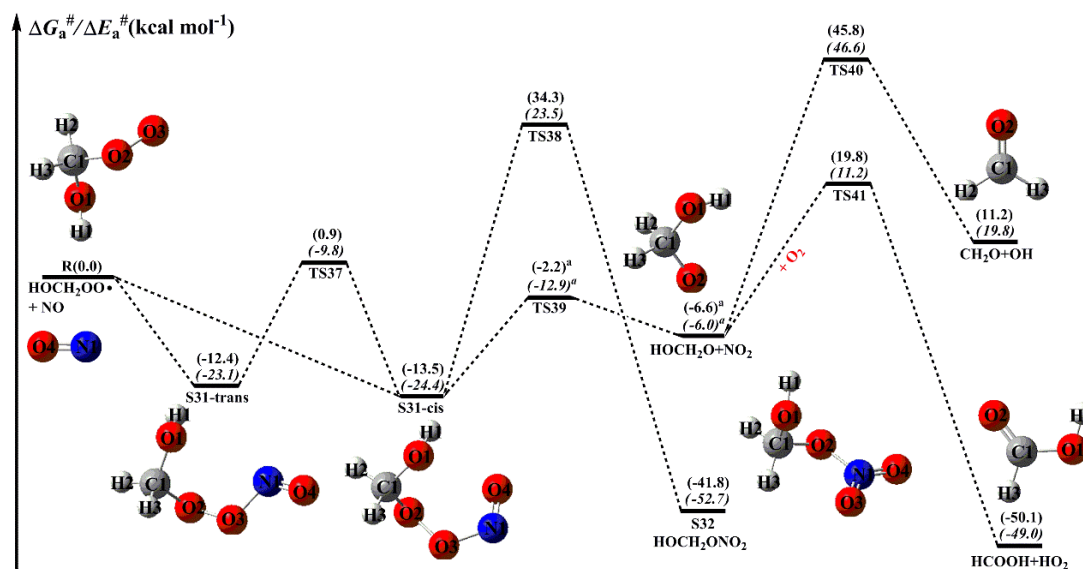
631 From Figure 11, it can be seen that the addition NO to HOCH(CH₃)OO radical
632 leading to the formation of S33-*cis* is barrierless. Then, it decomposes into
633 HOCH(CH₃)O radical and NO₂ (R44) via the cleavage of O₂-O₃ bond with the barrier
634 of 11.5 kcal mol⁻¹. The resulting HOCH(CH₃)O radical has three possible pathways.
635 The first one is β -site C₁-C₂ bond scission leading to the formation of HCOOH + CH₃
636 (R45) with the barrier of 8.3 kcal mol⁻¹. The second one is β -site C₁-O₁ bond cleavage
637 resulting in formation of CH₃COH + OH (R46) with the barrier of 26.7 kcal mol⁻¹.
638 The third one is H-abstraction by O₂ leading to CH₃COOH + HO₂ (R47) with the
639 barrier of 26.2 kcal mol⁻¹. Based on the calculated reaction barriers, it can be found
640 that β -site C₁-C₂ bond scission is the dominant pathway in the fragmentation of
641 HOCH(CH₃)O radical. This conclusion is further supported by the previous
642 experimental result that β -hydroxy intermediates primarily proceed decomposition
643 rather than react with O₂ in the presence of NO (Aschmann et al., 2000). Equivalent to
644 the HOCH(CH₃)OO + NO reaction, the bimolecular reaction of HO(CH₃)₂COO
645 radical with NO has similar transformation pathways (Figure 12). The reaction for
646 HO(CH₃)₂COO with NO initially proceeds via a barrierless addition leading to
647 S35-*cis* with the binding energy of 12.6 kcal mol⁻¹. Then, S35-*cis* fragments into
648 HO(CH₃)₂CO radical along with NO₂ (R50) via the cleavage of O₂-O₃ bond with the
649 barrier of 11.4 kcal mol⁻¹. The formed HO(CH₃)₂CO radical can either dissociate to
650 CH₃COOH + CH₃ (R51) via the C₁-C₃ bond scission with the barrier of 8.2 kcal mol⁻¹,
651 or decompose into CH₃COCH₃ + OH (R52) through the C₁-O₁ bond breaking with the
652 barrier of 24.3 kcal mol⁻¹. The result again shows that the β -site C-C bond scission is
653 the dominant pathway.

654 The typical atmospheric concentrations of NO are about 10 ppbv, 1 ppbv and 20
655 pptv in the urban, rural and forest environments (Bianchi et al., 2019). The rate
656 coefficient of HOCH₂OO radical reaction with NO is calculated to be 4.3×10^{-12} cm³
657 molecule⁻¹ s⁻¹ at room temperature, resulting in the pseudo-first-order rate constants
658 $k'_{\text{NO}} = k_{\text{NO}}[\text{NO}]$ of 6.5×10^{-1} , 6.5×10^{-2} , and 1.3×10^{-3} , respectively, in the urban,
659 rural and forest environments. It is of interest to assess the relative importance for the
660 H-shift reaction of HOCH₂OO radical and bimolecular reactions with HO₂ radical and

661 NO based on the calculated $k_{\text{MC-TST}}$, k'_{HO_2} and k'_{NO} . It can be found that the H-shift
 662 reaction is of less importance, the HO_2 radical reaction is favorable in the forest
 663 environments, while the NO reaction is predominant in the urban and rural regions.
 664 Similar conclusion is also obtained from the cases of $\text{HOCH}(\text{CH}_3)\text{OO}$ and
 665 $\text{HO}(\text{CH}_3)_2\text{CHOO}$ radicals.

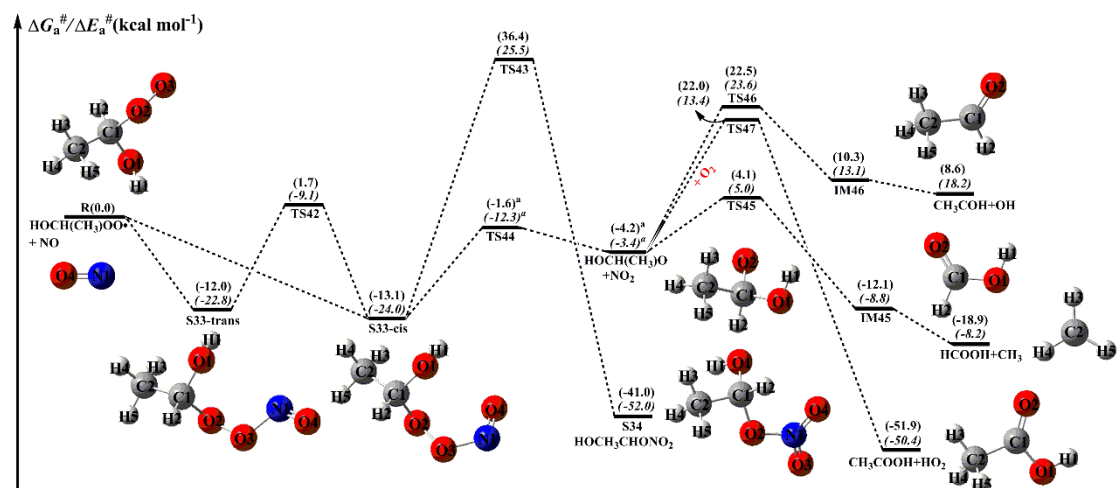
666 The rate coefficients of the dominant pathways of HOCH_2O , $\text{HOCH}(\text{CH}_3)\text{O}$ and
 667 $\text{HO}(\text{CH}_3)_2\text{CHO}$ radicals fragmentation are summarized in Table S12. As can be seen
 668 in Table S12, k_{R41} is slightly increased with the temperature increasing, and the
 669 discrepancy is about a factor of 12 at the two extremes of temperature. At ground
 670 level with $[\text{O}_2] \sim 5.0 \times 10^{18}$ molecule cm^{-3} , the pseudo-first-order rate constant k'_{O_2}
 671 $= k_{\text{R41}}[\text{O}_2]$ is estimated to be 38.0 s^{-1} at room temperature. k_{R45} vary significantly from
 672 2.0×10^6 (273 K) to 3.1×10^8 (400 K) s^{-1} , and they exhibit a marked positive
 673 temperature dependence. Similar phenomenon is also observed from k_{R51} that k_{R51} is
 674 significantly increased with increasing temperature. k_{R51} is a factor of ~ 1.3 greater
 675 than k_{R45} in the temperature range studied, implying that the rate coefficient of β -site
 676 C-C bond scission is slightly increased as the number of methyl group is increased.

677



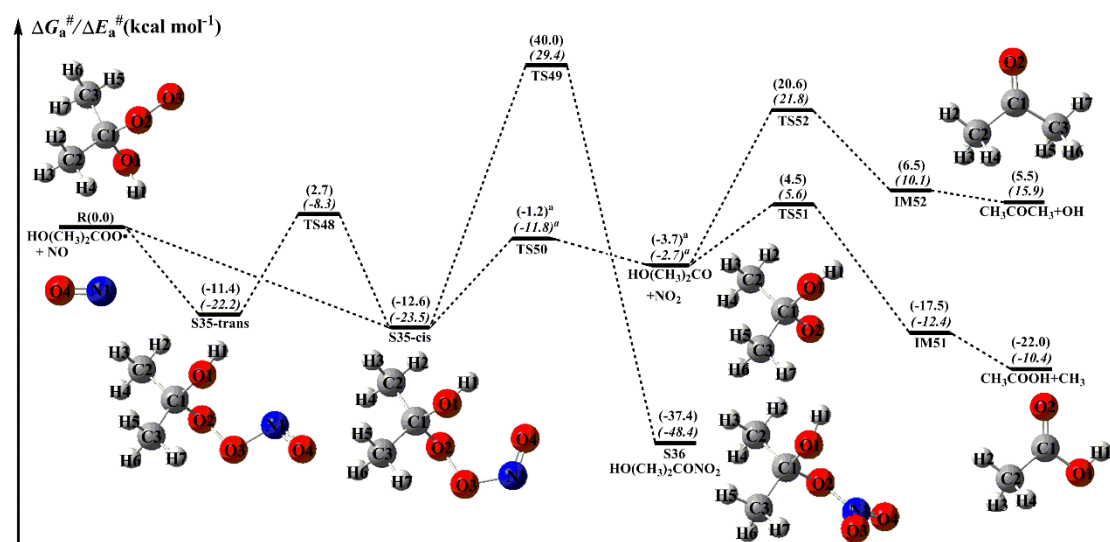
678

679 **Figure 10.** PES (ΔG_a^\ddagger and ΔE_a^\ddagger , in italics) for the reaction of HOCH_2OO radical with NO
 680 predicted at the M06-2X/ma-TZVP//M06-2X/6-311+G(2df,2p) level of theory (the superscript a is
 681 calculated at the MP2/ma-TZVP//MP2/6-311+G(2df,2p) level)



682

683 **Figure 11.** PES (ΔG_a^\ddagger and ΔE_a^\ddagger , in italics) for the reaction of HOCH(CH₃)OO radical with NO
 684 predicted at the M06-2X/ma-TZVP//M06-2X/6-311+G(2df,2p) level of theory (the superscript a is
 685 calculated at the MP2/ma-TZVP//MP2/6-311+G(2df,2p) level)



686

687 **Figure 12.** PES (ΔG_a^\ddagger and ΔE_a^\ddagger , in italics) for the reaction of HO(CH₃)₂COO radical with NO
 688 predicted at the M06-2X/ma-TZVP//M06-2X/6-311+G(2df,2p) level of theory (the superscript a is
 689 calculated at the MP2/ma-TZVP//MP2/6-311+G(2df,2p) level)

690 4. Conclusions

691 The detailed mechanisms and kinetic properties of OH-initiated oxidation of
 692 distinct HHPs and subsequent transformation of resulting H-abstraction products are
 693 investigated using quantum chemical and kinetics modeling methods. The main
 694 conclusions are summarized as follows:

- 695 (a) The dominant pathway is the H-abstraction from the -OOH group in the
 696 initiation reactions of OH radical with HOCH₂OOH and HOC(CH₃)₂OOH.
 697 H-abstraction from the -CH group is competitive with that from the -OOH group in

698 the reaction of OH radical with HOCH(CH₃)OOH. The barrier of H-abstraction from
699 the -OOH group is slightly increased as the number of methyl group is increased.
700 Compared with the rate coefficient of dominant pathway in the parent system, it is
701 almost identical when a methyl group substitution occurs at the C₁-position, whereas
702 it reduces by a factor of 2-5 when two methyl groups are introduced into the
703 C₁-position. The atmospheric lifetime of HOCH₂OOH, HOCH(CH₃)OOH and
704 HOC(CH₃)₂OOH reactivity toward OH radical are estimated to be 0.58-1.74 h,
705 0.60-1.79 h and 1.23-3.69 h at room temperature under the typical OH radical
706 concentrations of 5-15 × 10⁶ molecules cm⁻³ during daylight.

707 (b) The self-reaction of H-abstraction product RO₂ radical initially produces
708 tetroxide intermediate via an oxygen-to-oxygen coupling, then it decomposes into
709 propagation and termination products through the asymmetric two-step O-O bond
710 scission. The rate-limiting step is the first O-O bond cleavage, and the barrier is
711 increased with increasing the number of methyl group. This finding is meaningful to
712 understand the self-reaction of complex RO₂ radicals.

713 (c) The bimolecular reactions of distinct RO₂ radicals with HO₂ radical lead to
714 the formation of hydroperoxide ROOH as the main product, and the barrier height is
715 independent on the number of methyl substitution. When compared to the rate
716 coefficient for HOCH₂OO + HO₂ reaction, the rate coefficients increase by a factor of
717 2-5 when one or two methyl groups are introduced into the C1-position. Using a HO₂
718 radical concentration of ~50 pptv in the forest environments, the pseudo-first-order
719 rate constants k'_{HO_2} of distinct RO₂ radical reactions with HO₂ radical vary from 1 to 5
720 × 10⁻² s⁻¹.

721 (d) The isomerization reactions of HOCH₂OO, HOCH(CH₃)OO and
722 HO(CH₃)₂COO radicals are unlikely to proceed in the atmosphere because the
723 intramolecular H-shift steps have dramatically high barriers and strongly endergonic.
724 The result implies that the isomerization of RO₂ radicals with smaller carbon
725 structures is of less importance in the atmosphere.

726 (e) Reaction with O₂ forming formic acid and HO₂ radical is the dominant
727 removal pathway for HOCH₂O radical formed from the reaction of HOCH₂OO

728 radical with NO. The β -site C-C bond scission is the dominant pathway in the
729 dissociation of HOCH(CH₃)O and HOC(CH₃)₂O radicals formed from the reactions
730 of NO with HOCH(CH₃)OO and HOC(CH₃)₂OO radicals. The result implies that the
731 methyl-substituted alkoxy radicals primarily proceed via β -site C-C bond scission to
732 produce aldehyde rather than react with O₂.

733

734 **Data availability**

735 The data are accessible by contacting the corresponding author
736 (huangyu@ieecas.cn).

737 **Supplement**

738 The following information is provided in the Supplement: Y//X (Y = M06-2X,
739 CCSD(T), X = 6-311+G(2df,2p), ma-TZVP) calculated energy barrier ($\Delta E_a^\#$, $\Delta G_a^\#$)
740 for OH + HHPs reactions; Rate coefficients of every elementary pathway involved in
741 the initial reactions of OH radical with HOCH₂OOH, HOCH(CH₃)OOH and
742 HO(CH₃)₂COOH; Rate coefficients of HO₂ radical reactions with HOCH₂OO,
743 HOCH(CH₃)OO and HO(CH₃)₂COO radicals; The relative free energy and
744 Boltzmann populations (w_i) of the conformer of HOCH₂OO, HOCH(CH₃)OO and
745 HO(CH₃)₂COO radicals; The single-conformer rate coefficients ($k_{\text{IRC-TST}}$) and
746 multi-conformer rate coefficients ($k_{\text{MC-TST}}$) of HOCH₂OO, HOCH(CH₃)OO and
747 HO(CH₃)₂COO radicals; Rate coefficients of dominant pathways in the HOCH₂OO · +
748 NO, HOCH(CH₃)OO · + NO and HO(CH₃)₂CHOO · + NO reactions; PESs ($\Delta E_a^\#$) for
749 the OH-initiated reactions of HOCH₂OOH, HOCH(CH₃)OOH, HOC(CH₃)₂OOH;
750 Geometries of all the stationary points; Plots of the rate coefficients of every
751 elementary pathway versus temperature; PESs ($\Delta G_a^\#$ and $\Delta E_a^\#$, in italics) for the
752 isomerization of HOCH(CH₃)OO and HO(CH₃)₂COO radicals.

753

754 **Author contribution**

755 LC designed the study. LC and YH wrote the paper. LC performed theoretical

756 calculation. YX, ZJ, and WW analyzed the data. All authors reviewed and commented
757 on the paper.

758

759 **Competing interests**

760 The authors declare that they have no conflict of interest.

761

762 **Acknowledgments**

763 This work was supported by the National Natural Science Foundation of China
764 (grant Nos. 42175134, 41805107, and 22002080). It was also partially supported as
765 Key Projects of Chinese Academy of Sciences, China (grant No. ZDRW-ZS-2017-6),
766 Strategic Priority Research Program of the Chinese Academy of Sciences, China
767 (grant Nos. XDA23010300 and XDA23010000), Key Project of International
768 Cooperation of the Chinese Academy of Sciences, China (grant No. GJHZ1543),
769 Research Grants Council of Hong Kong, China (grant No. PolyU 152083/14E), CAS
770 "Light of West China" Program (XAB2019B01) and the General Project of Shaanxi
771 Province (2020JQ-432).

772

773 **References**

- 774 Allen, H. M., Crouse, J. D., Bates, K. H., Teng, A. P., Krawiec-Thayer, M. P., Rivera-Rios, J. C.,
775 Keutsch, F. N., Clair, J. M. S., Hanisco, T. F., Møller, K. H., Kjaergaard, H. G., and Wennberg,
776 P. O.: Kinetics and product yields of the OH initiated oxidation of hydroxymethyl
777 hydroperoxide, *J. Phys. Chem. A*, 122, 6292-6302, <https://doi.org/10.1021/acs.jpca.8b04577>,
778 2018.
- 779 Anglada, J. M., and Solé A.: Impact of the water dimer on the atmospheric reactivity of carbonyl
780 oxides, *Phys. Chem. Chem. Phys.*, 18, 17698-17712, <https://doi.org/10.1039/C6CP02531E>,
781 2016.
- 782 Anglada, J. M., González, J., and Torrent-Sucarrat, M.: Effects of the substituents on the reactivity
783 of carbonyl oxides. a theoretical study on the reaction of substituted carbonyl oxides with
784 water, *Phys. Chem. Chem. Phys.*, 13, 13034-13045, <https://doi.org/10.1039/c1cp20872a>,
785 2011.
- 786 Aschmann, S. M., Arey, J., and Atkinson, R.: Formation of β -hydroxycarbonyls from the OH
787 radical-initiated reactions of selected alkenes, *Environ. Sci. Technol.*, 34, 1702-1706,
788 <https://doi.org/10.1021/es991125a>, 2000.

789 Atkinson, R., and Arey, J.: Atmospheric degradation of volatile organic compounds, *Chem. Rev.*,
790 103, 4605-4638, <https://doi.org/10.1021/cr0206420>, 2003.

791 Bach, R. D., Dmitrenko, O., and Estévez, C. M.: Chemical behavior of the biradicaloid
792 (HO ··ONO) singlet states of peroxyoxynitrous acid. the oxidation of hydrocarbons, sulfides, and
793 selenides, *J. Am. Chem. Soc.*, 127, 3140-3155, <https://doi.org/10.1021/ja044245d>, 2005.

794 Berndt, T., Richters, S., Kaethner, R., Voigtländer, J., Stratmann, F., Sipilä M., Kulmala, M., and
795 Herrmann, H.: Gas-phase ozonolysis of cycloalkenes: formation of highly oxidized RO₂ radicals
796 and their reactions with NO, NO₂, SO₂, and Other RO₂ radicals, *J. Phys. Chem. A*, 119,
797 10336-10348, <https://doi.org/10.1021/acs.jpca.5b07295>, 2015.

798 Berndt, T., Scholz, W., Mentler, B., Fischer, L., Herrmann, H., Kulmala, M., and Hansel, A.:
799 Accretion product formation from self- and cross-reactions of RO₂ radicals in the atmosphere,
800 *Angew. Chem. Int. Ed.*, 57, 3820-3824, <https://doi.org/10.1002/anie.201710989>, 2018.

801 Bianchi, F., Kurten, T., Riva, M., Mohr, C., Rissanen, M. P., Roldin, P., Berndt, T., Crouse, J. D.,
802 Wennberg, P. O., Mentel, T. F., Wildt, J., Junninen, H., Jokinen, T., Kulmala, M., Worsnop, D.
803 R., Thornton, J. A., Donahue, N., Kjaergaard, H. G., and Ehn, M.: Highly oxygenated organic
804 molecules (HOM) from gas-phase autoxidation involving peroxy radicals: a key contributor
805 to atmospheric aerosol, *Chem. Rev.*, 119, 3472-3509,
806 <https://doi.org/10.1021/acs.chemrev.8b00395>, 2019.

807 Boys, S. F., and Bernardi, F.: The calculation of small molecular interactions by the differences of
808 separate total energies. Some procedures with reduced errors, *Mol. Phys.*, 19, 553-566,
809 <https://doi.org/10.1080/00268977000101561>, 1970.

810 Chao, W., Hsieh, J. T., Chang, C. H., and Lin, J. J. M.: Direct kinetic measurement of the reaction
811 of the simplest Criegee intermediate with water vapor, *Science*, 347, 751-754,
812 <https://doi.org/10.1126/science.1261549>, 2015.

813 Chen, L., Huang, Y., Xue, Y., Cao, J., and Wang, W.: Competition between HO₂ and H₂O₂
814 reactions with CH₂OO/*anti*-CH₃CHOO in the oligomer formation: a theoretical perspective, *J.*
815 *Phys. Chem. A*, 121, 6981-6991, <https://doi.org/10.1021/acs.jpca.7b05951>, 2017.

816 Chen, L., Huang, Y., Xue, Y., Jia, Z., and Wang, W.: Atmospheric oxidation of 1-butene initiated
817 by OH radical: Implications for ozone and nitrous acid formations, *Atmos. Environ.*, 244,
818 118010-118021, <https://doi.org/10.1016/j.atmosenv.2020.118010>, 2021.

819 Chen, L., Huang, Y., Xue, Y., Shen, Z., Cao, J., and Wang, W.: Mechanistic and kinetics
820 investigations of oligomer formation from Criegee intermediate reactions with hydroxyalkyl
821 hydroperoxides, *Atmos. Chem. Phys.*, 19, 4075-4091,
822 <https://doi.org/10.5194/acp-19-4075-2019>, 2019.

823 Chen, L., Wang, W., Wang, W., Liu, Y., Liu, F., Liu, N., and Wang, B.: Water-catalyzed
824 decomposition of the simplest Criegee intermediate CH₂OO, *Theor. Chem. Acc.*, 135,
825 131-143, <https://doi.org/10.1007/s00214-016-1894-9>, 2016b.

826 Chen, L., Wang, W., Zhou, L., Wang, W., Liu, F., Li, C., and Lü, J.: Role of water clusters in the
827 reaction of the simplest Criegee intermediate CH₂OO with water vapour, *Theor. Chem. Acc.*,
828 135, 252-263, <https://doi.org/10.1007/s00214-016-1998-2>, 2016a.

829 Chhantyal-Pun, R., Welz, O., Savee, J. D., Eskola, A. J., Lee, E. P. F., Blacker, L., Hill, H. R.,
830 Ashcroft, M., Khan, M. A. H., Lloyd-Jones, G. C., Evans, L., Rotavera, B., Huang, H.,
831 Osborn, D. L., Mok, D. K. W., Dyke, J. M., Shallcross, D. E., Percival, C. J., Orr-Ewing, A. J.,
832 and Taatjes, C. A.: Direct measurements of unimolecular and bimolecular reaction kinetics of

833 the Criegee intermediate $(\text{CH}_3)_2\text{COO}$, *J. Phys. Chem. A*, 121, 4-15,
834 <https://doi.org/10.1021/acs.jpca.6b07810>, 2017.

835 Crounse, J. D., Nielsen, L. B., Jørgensen, S., Kjaergaard, H. G., and Wennberg, P. O.:
836 Autoxidation of organic compounds in the atmosphere, *J. Phys. Chem. Lett.*, 4, 3513-3520,
837 <https://doi.org/10.1021/jz4019207>, 2013.

838 Dillon, T. J., and Crowley, J. N.: Direct detection of OH formation in the reactions of HO_2 with
839 $\text{CH}_3\text{C}(\text{O})\text{O}_2$ and other substituted peroxy radicals, *Atmos. Chem. Phys.*, 8, 4877-4889,
840 <https://doi.org/10.5194/acp-8-4877-2008>, 2008.

841 Eckart, C.: The penetration of a potential barrier by electrons, *Phys. Rev.*, 35, 1303-1309,
842 <https://doi.org/10.1103/PhysRev.35.1303>, 1930.

843 Ehn, M., Berndt, T., Wildt, J., and Mentel, T.: Highly oxygenated molecules from atmospheric
844 autoxidation of hydrocarbons: a prominent challenge for chemical kinetics studies, *Int. J.*
845 *Chem. Kinet.*, 49, 821-831, <https://doi.org/10.1002/kin.21130>, 2017.

846 Ehn, M., Thornton, J. A., Kleist, E., Sipilä M., Junninen, H., Pullinen, I., Springer, M., Rubach, F.,
847 Tillmann, R., Lee, B., Lopez-Hilfiker, F., Andres, S., Acir, I. H., Rissanen, M., Jokinen, T.,
848 Schobesberger, S., Kangasluoma, J., Kontkanen, J., Nieminen, T., Kurtén, T., Nielsen, L. B.,
849 Jørgensen, S., Kjaergaard, H. G., Canagaratna, M., Maso, M. D., Berndt, T., Petäjä T.,
850 Wahner, A., Kerminen, V. M., Kulmala, M., Worsnop, D. R., Wildt, J., and Mentel T. F.: A
851 large source of low-volatility secondary organic aerosol, *Nature*, 506, 476-479,
852 <https://doi.org/10.1038/nature13032>, 2014.

853 Fernández-Ramos, A., Ellingson, B. A., Meana-Pañeda, R., Marques, J. M. C., and Truhlar, D. G.:
854 Symmetry numbers and chemical reaction rates, *Theor. Chem. Acc.*, 118, 813-826,
855 <https://doi.org/10.1007/s00214-007-0328-0>, 2007.

856 Francisco, J. S., and Eisfeld, W.: Atmospheric oxidation mechanism of hydroxymethyl
857 hydroperoxide, *J. Phys. Chem. A*, 113, 7593-7600, <https://doi.org/10.1021/jp901735z>, 2009.

858 Frisch, M. J., Trucks, G. W., Schlegel, H. B., Scuseria, G. E., Robb, M. A., Cheeseman, J. R.,
859 Montgomery, J. A. Jr., Vreven, T., Kudin, K. N., Burant, J. C., Millam, J. M., Iyengar, S. S.,
860 Tomasi, J., Barone, V., Mennucci, B., Cossi, M., Scalmani, G., Rega, N., Petersson, G. A.,
861 Nakatsuji, H., Hada, M., Ehara, M., Toyota, K., Fukuda, R., Hasegawa, J., Ishida, M.,
862 Nakajima, T., Honda, Y., Kitao, O., Nakai, H., Klene, M., Li, X., Knox, J. E., Hratchian, H. P.,
863 Cross, J. B., Adamo, C., Jaramillo, J., Gomperts, R., Stratmann, R. E., Yazyev, O., Austin, A.
864 J., Cammi, R., Pomelli, C., Ochterski, J. W., Ayala, P. Y., Morokuma, K., Voth, G. A.,
865 Salvador, P., Dannenberg, J. J., Zakrzewski, V. G., Dapprich, S., Daniels, A. D., Strain, M. C.,
866 Farkas, O., Malick, D. K., Rabuck, A. D., Raghavachari, K., Foresman, J. B., Ortiz, J. V., Cui,
867 Q., Baboul, A. G., Clifford, S., Cioslowski, J., Stefanov, B. B., Liu, G., Liashenko, A.,
868 Piskorz, P., Komaromi, I., Martin, R. L., Fox, D. J., Keith, T., Al-Laham, M. A., Peng, C. Y.,
869 Nanayakkara, A., Challacombe, M., Gill, P. M. W., Johnson, B., Chen, W., Wong, M. W.,
870 Gonzalez, C., and Pople, J. A.: Gaussian 09, Revision D.01; Gaussian, Inc.: Wallingford, CT,
871 2009.

872 Fukui, K.: The path of chemical reactions - the IRC approach, *Acc. Chem. Res.*, 14, 363-368,
873 <https://doi.org/10.1021/ar00072a001>, 1981.

874 Gilbert, R. G., and Smith, S. C.: Theory of unimolecular and recombination reactions; Blackwell
875 Scientific: Carlton, Australia, 1990.

876 Gligorovski, S., Strekowski, R., Barbati, S., and Vione, D.: Environmental implications of

877 hydroxyl radicals (OH), *Chem. Rev.*, 115, 13051-13092, <https://doi.org/10.1021/cr500310b>,
878 2015.

879 Glowacki, D. R., Liang, C. H., Morley, C., Pilling, M. J., and Robertson, S. H.: MESMER: an
880 open-source master equation solver for multi-energy well reactions, *J. Phys. Chem. A*, 116,
881 9545-9560, <https://doi.org/10.1021/jp3051033>, 2012.

882 Gong, Y., and Chen, Z.: Quantification of the role of stabilized Criegee intermediates in the
883 formation of aerosols in limonene ozonolysis, *Atmos. Chem. Phys.*, 21, 813-829,
884 <https://doi.org/10.5194/acp-21-813-2021>, 2021.

885 Hofzumahaus, A., Rohrer, F., Lu, K., Bohn, B., Brauers, T., Chang, C. C., Fuchs, H., Holland, F.,
886 Kita, K., Kondo, Y., Li, X., Lou, S., Shao, M., Zeng, L., Wahner, A., and Zhang, Y.:
887 Amplified trace gas removal in the troposphere, *Science*, 324, 1702-1704,
888 <https://doi.org/10.1126/science.1164566>, 2009.

889 Holbrook, K. A., Pilling, M. J., Robertson, S. H., and Robinson, P. J.: *Unimolecular reactions*, 2nd
890 ed.; Wiley: New York, 1996.

891 Huang, H. L., Chao, W., and Lin, J. J. M.: Kinetics of a Criegee intermediate that would survive
892 high humidity and may oxidize atmospheric SO₂, *Proc. Natl. Acad. Sci. U.S.A.*, 112,
893 10857-10862, <https://doi.org/10.1073/pnas.1513149112>, 2015.

894 Iyer, S., Reiman, H., Møller, K. H., Rissanen, M. P., Kjaergaard, H. G., and Kurtén, T.:
895 Computational investigation of RO₂ + HO₂ and RO₂ + RO₂ reactions of monoterpene derived
896 first-generation peroxy radicals leading to radical recycling, *J. Phys. Chem. A*, 122,
897 9542-9552, <https://doi.org/10.1021/acs.jpca.8b09241>, 2018.

898 Iyer, S., Rissanen, M. P., Valiev, R., Barua, S., Krechmer, J. E., Thornton, J., Ehn, M., and Kurtén,
899 T.: Molecular mechanism for rapid autoxidation in α -pinene ozonolysis, *Nat. Commun.*,
900 <https://doi.org/10.1038/s41467-021-21172-w>, 12, 878-883, 2021.

901 Jara-Toro, R. A., Hernández, F. J., Garavagno, M. A., Taccone, R. A., and Pino, G. A.: Water
902 catalysis of the reaction between hydroxyl radicals and linear saturated alcohols (ethanol and
903 n-propanol) at 294 K, *Phys. Chem. Chem. Phys.*, 20, 27885-27896,
904 <https://doi.org/10.1039/C8CP05411H>, 2018.

905 Jara-Toro, R. A., Hernández, F. J., Taccone, R. A., Lane, S. I., and Pino, G. A.: Water catalysis of
906 the reaction between methanol and OH at 294 K and the atmospheric implications, *Angew.
907 Chem., Int. Ed.*, 56, 2166-2170, <https://doi.org/10.1002/anie.201612151>, 2017.

908 Jokinen, T., Sipilä M., Richters, S., Kerminen, V. M., Paasonen, P., Stratmann, F., Worsnop, D.,
909 Kulmala, M., Ehn, M., Herrmann, H., and Berndt, T.: Rapid autoxidation forms highly
910 oxidized RO₂ radicals in the atmosphere, *Angew. Chem. Int. Ed.*, 53, 14596-14600,
911 <https://doi.org/10.1002/anie.201408566>, 2014.

912 Khan, M. A. H., Percival, C. J., Caravan, R. L., Taatjes, C. A., and Shallcross, D. E.: Criegee
913 intermediates and their impacts on the troposphere, *Environ. Sci.: Processes Impacts*, 20,
914 437-453, <https://doi.org/10.1039/C7EM00585G>, 2018.

915 Kumar, M., and Francisco, J. S.: Red-light initiated decomposition of α -hydroxy methylperoxy
916 radical in the presence of organic and inorganic acids: implications for the HO_x formation in
917 the lower stratosphere, *J. Phys. Chem. A*, 120, 2677-2683,
918 <https://doi.org/10.1021/acs.jpca.6b01515>, 2016.

919 Kumar, M., and Francisco, J. S.: Red-light-induced decomposition of an organic peroxy radical: a
920 new source of the HO₂ radical, *Angew. Chem. Int. Ed.*, 54, 15711-15714,

921 <https://doi.org/10.1002/anie.201509311>, 2015.

922 Kumar, M., Busch, D. H., Subramaniam, Bala., and Thompson, W. H.: Role of tunable acid
923 catalysis in decomposition of α -hydroxyalkyl hydroperoxides and mechanistic implications
924 for tropospheric chemistry, *J. Phys. Chem. A*, 118, 9701-9711,
925 <https://doi.org/10.1021/jp505100x>, 2014.

926 Lee, R., Gryn'ova, G., Ingold, K. U., and Coote, M. L.: Why are sec-alkylperoxyl bimolecular
927 self-reactions orders of magnitude faster than the analogous reactions of tert-alkylperoxyls?
928 The unanticipated role of CH hydrogen bond donation, *Phys. Chem. Chem. Phys.*, 18,
929 23673-23679, <https://doi.org/10.1039/C6CP04670C>, 2016.

930 Lester, M. I., and Klippenstein, S. J.: Unimolecular decay of Criegee intermediates to OH radical
931 products: prompt and thermal decay processes, *Acc. Chem. Res.*, 51, 978-985,
932 <https://doi.org/10.1021/acs.accounts.8b00077>, 2018.

933 Liu, L., Bei, N., Wu, J., Liu, S., Zhou, J., Li, X., Yang, Q., Feng, T., Cao, J., Tie, X., and Li, G.:
934 Effects of stabilized Criegee intermediates (sCIs) on sulfate formation: a sensitivity analysis
935 during summertime in Beijing-Tianjin-Hebei (BTH), China. *Atmos. Chem. Phys.*, 19,
936 13341-13354, <https://doi.org/10.5194/acp-19-13341-2019>, 2019.

937 Long, B., Bao, J. L., and Truhlar, D. G.: Reaction of SO₂ with OH in the atmosphere, *Phys. Chem.*
938 *Chem. Phys.*, 19, 8091-8100, <https://doi.org/10.1039/C7CP00497D>, 2017.

939 Lu, T.: Molclus program, Version 1.9.3, <http://www.keinsci.com/research/molclus.html> (accessed
940 Feb. 10, 2020).

941 Ma, F., Guo, X., Xia, D., Xie, H. B., Wang, Y., Elm, J., Chen, J., and Niu, J.: Atmospheric
942 chemistry of allylic radicals from isoprene: a successive cyclization-driven autoxidation
943 mechanism, *Environ. Sci. Technol.*, 55, 4399-4409, <https://doi.org/10.1021/acs.est.0c07925>,
944 2021.

945 Møller, K. H., Berndt, T., and Kjaergaard, H. G.: Atmospheric autoxidation of amines, *Environ.*
946 *Sci. Technol.*, 54, 11087-11099, <https://doi.org/10.1021/acs.est.0c03937>, 2020.

947 Møller, K. H., Otkjær, R. V., Hyttinen, N., Kurtán, T., and Kjaergaard, H. G.: Cost-effective
948 implementation of multiconformer transition state theory for peroxy radical hydrogen shift
949 reactions, *J. Phys. Chem. A*, 120, 10072-10087, <https://doi.org/10.1021/acs.jpca.6b09370>,
950 2016.

951 Nozière, B., and Vereecken, L.: Direct observation of aliphatic peroxy radical autoxidation and
952 water effects: an experimental and theoretical study, *Angew. Chem. Int. Ed.*, 58, 13976-13982,
953 <https://doi.org/10.1002/anie.201907981>, 2019.

954 Orlando, J. J., and Tyndall, G. S.: Laboratory studies of organic peroxy radical chemistry: an
955 overview with emphasis on recent issues of atmospheric significance, *Chem. Soc. Rev.*, 41,
956 6294-6317, <https://doi.org/10.1039/c2cs35166h>, 2012.

957 Perring, A. E., Pusede, S. E., and Cohen, R. C.: An observational perspective on the atmospheric
958 impacts of alkyl and multifunctional nitrates on ozone and secondary organic aerosol, *Chem.*
959 *Rev.*, 113, 5848-5870, <https://doi.org/10.1021/cr300520x>, 2013.

960 Piletic, I. R., Edney, E. O., and Bartolotti, L. J.: Barrierless reactions with loose transition states
961 govern the yields and lifetimes of organic nitrates derived from isoprene, *J. Phys. Chem. A*,
962 121, 8306-8321, <https://doi.org/10.1021/acs.jpca.7b08229>, 2017.

963 Qiu, J. T., Ishizuka, S., Tonokura, K., Colussi, A. J., and Enami, S.: Water dramatically accelerates
964 the decomposition of α -hydroxyalkyl-hydroperoxides in aerosol particles, *J. Phys. Chem.*

965 Lett., 10, 5748-5755, <https://doi.org/10.1021/acs.jpcelett.9b01953>, 2019.

966 Rissanen, M. P., Kurtšn, T., Sipilä M., Thornton, J. A., Kangasluoma, J., Sarnela, N., Junninen, H.,
967 Jørgensen, S., Schallhart, S., Kajos, M. K., Taipale, R., Springer, M., Mentel, T. F.,
968 Ruuskanen, T., Petäjä T., Worsnop, D. R., Kjaergaard, H. G., and Ehn, M.: The formation of
969 highly oxidized multifunctional products in the ozonolysis of cyclohexene, *J. Am. Chem.*
970 *Soc.*, 136, 15596-15606, <https://doi.org/10.1021/ja507146s>, 2014.

971 Russell, G. A.: Deuterium-isotope effects in the autoxidation of aralkyl hydrocarbons. Mechanism
972 of the interaction of peroxy radicals, *J. Am. Chem. Soc.*, 79, 3871-3877,
973 <https://doi.org/10.1021/ja01571a068>, 1957.

974 Ryzhkov, A. B., and Ariya, P. A.: A theoretical study of the reactions of carbonyl oxide with water
975 in atmosphere: the role of water dimer, *Chem. Phys. Lett.*, 367, 423-429,
976 [https://doi.org/10.1016/S0009-2614\(02\)01685-8](https://doi.org/10.1016/S0009-2614(02)01685-8), 2003.

977 Smith, M. C., Chang, C. H., Chao, W., Lin, L. C., Takahashi, K., Boering, K. A., and Lin, J. J. M.:
978 Strong negative temperature dependence of the simplest Criegee intermediate CH_2OO
979 reaction with water dimer, *J. Phys. Chem. Lett.*, 6, 2708-2713,
980 <https://doi.org/10.1021/acs.jpcelett.5b01109>, 2015.

981 Stone, D., Whalley, L. K., and Heard, D. E.: Tropospheric OH and HO_2 radicals: field
982 measurements and model comparisons, *Chem. Soc. Rev.*, 41, 6348-6404,
983 <https://doi.org/10.1039/c2cs35140d>, 2012.

984 Taatjes, C. A., Welz, O., Eskola, A. J., Savee, J. D., Scheer, A. M., Shallcross, D. E., Rotavera, B.,
985 Lee, E. P. F., Dyke, J. M., Mok, D. K. W., Osborn, D. L., and Percival, C. J.: Direct
986 measurements of conformer-dependent reactivity of the Criegee intermediate CH_3CHOO ,
987 *Science*, 340, 177-180, <https://doi.org/10.1126/science.1234689>, 2013.

988 Taatjes, C. A.: Criegee intermediates: what direct production and detection can teach us about
989 reactions of carbonyl oxides, *Annu. Rev. Phys. Chem.*, 68, 183-207,
990 <https://doi.org/10.1146/annurev-physchem-052516-050739>, 2017.

991 Valiev, R. R., Hasan, G., Salo, V. T., Kubečka, J., and Kurten, T.: Intersystem crossings drive
992 atmospheric gas-phase dimer formation, *J. Phys. Chem. A*, 123, 6596-6604,
993 <https://doi.org/10.1021/acs.jpca.9b02559>, 2019.

994 Wang, S., Riva, M., Yan, C., Ehn, M., and Wang, L.: Primary formation of highly oxidized
995 multifunctional products in the OH-initiated oxidation of isoprene: a combined theoretical
996 and experimental study, *Environ. Sci. Technol.*, 52, 12255-12264,
997 <https://doi.org/10.1021/acs.est.8b02783>, 2018.

998 Wang, S., Wu, R., Berndt, T., Ehn, M., and Wang, L.: Formation of highly oxidized radicals and
999 multifunctional products from the atmospheric oxidation of alkylbenzenes, *Environ. Sci.*
1000 *Technol.*, 51, 8442-8449, <https://doi.org/10.1021/acs.est.7b02374>, 2017.

1001 Wennberg, P. O., Bates, K. H., Crouse, J. D., Dodson, L. G., McVay, R. C., Mertens, L. A.,
1002 Nguyen, T. B., Praske, E., Schwantes, R. H., Smarte, M. D., Clair, J. M. S., Teng, A. P.,
1003 Zhang, X., and Seinfeld, J. H.: Gas-phase reactions of isoprene and its major oxidation
1004 products, *Chem. Rev.*, 118, 3337-3390, <https://doi.org/10.1021/acs.chemrev.7b00439>, 2018.

1005 Winiberg, F. A. F., Dillon, T. J., Orr, S. C., Groß C. B. M., Bejan, I., Brumby, C. A., Evans, M. J.,
1006 Smith, S. C., Heard, D. E., and Seakins, P. W.: Direct measurements of OH and other product
1007 yields from the $\text{HO}_2 + \text{CH}_3\text{C}(\text{O})\text{O}_2$ reaction, *Atmos. Chem. Phys.*, 16, 4023-4042,
1008 <https://doi.org/10.5194/acp-16-4023-2016>, 2016.

1009 Xu, L., Kollman, M. S., Song, C., Shilling, J. E., and Ng, N. L.: Effects of NO_x on the volatility of
1010 secondary organic aerosol from isoprene photooxidation, *Environ. Sci. Technol.*, 48,
1011 2253-2262, <https://doi.org/10.1021/es404842g>, 2014.

1012 Xu, L., Møller, K. H., Crounse, J. D., Kjaergaard, H. G., and Wennberg, P. O.: New insights into
1013 the radical chemistry and product distribution in the OH-initiated oxidation of benzene,
1014 *Environ. Sci. Technol.*, 54, 13467-13477, <https://doi.org/10.1021/acs.est.0c04780>, 2020.

1015 Zhang, D., Zhang, R., Park, J., and North, S. W.: Hydroxy peroxy nitrites and nitrates from OH
1016 initiated reactions of isoprene, *J. Am. Chem. Soc.*, 124, 9600-9605,
1017 <https://doi.org/10.1021/ja0255195>, 2002.

1018 Zhang, P., Wang, W., Zhang, T., Chen, L., Du, Y., Li, C., and Lv, J.: Theoretical study on the
1019 mechanism and kinetics for the self-reaction of C₂H₅O₂ radicals, *J. Phys. Chem. A*, 116,
1020 4610-4620, <https://doi.org/10.1021/jp301308u>, 2012.

1021 Zhao, Y., and Truhlar, D. G.: A new local density functional for main-group thermochemistry,
1022 transition metal bonding, thermochemical kinetics, and noncovalent interactions, *J. Chem.*
1023 *Phys.*, 125, 194101-194119, <https://doi.org/10.1063/1.2370993>, 2006.

1024 Zhao, Y., and Truhlar, D. G.: The M06 suite of density functionals for main group
1025 thermochemistry, thermochemical kinetics, noncovalent interactions, excited states, and
1026 transition elements: two new functionals and systematic testing of four M06-class functionals
1027 and 12 other functionals, *Theor. Chem. Acc.*, 120, 215-241,
1028 <https://doi.org/10.1007/s00214-007-0310-x>, 2008.

1029 Zheng, J., and Truhlar, D. G.: Direct dynamics study of hydrogen-transfer isomerization of
1030 1-pentyl and 1-hexyl radicals, *J. Phys. Chem. A*, 113, 11919-11925,
1031 <https://doi.org/10.1021/jp903345x>, 2009.

1032 Zheng, J., Xu, X., and Truhlar, D. G.: Minimally augmented Karlsruhe basis sets, *Theor. Chem.*
1033 *Acc.*, 128, 295-305, <https://doi.org/10.1007/s00214-010-0846-z>, 2011.

1034 Zhong, J., Kumar, M., Francisco, J. S., and Zeng, X. C.: Insight into chemistry on cloud/aerosol
1035 water surfaces, *Acc. Chem. Res.*, 51, 1229-1237,
1036 <https://doi.org/10.1021/acs.accounts.8b00051>, 2018.

1037 Zhou, X., Liu, Y., Dong, W., and Yang, X.: Unimolecular reaction rate measurement of
1038 *syn*-CH₃CHOO, *J. Phys. Chem. Lett.*, 10, 4817-4821,
1039 <https://doi.org/10.1021/acs.jpcllett.9b01740>, 2019.

1040 Zhu, C., Kumar, M., Zhong, J., Li, L., Francisco, J. S., and Zeng, X. C.: New mechanistic
1041 pathways for Criegee-water chemistry at the air/water interface, *J. Am. Chem. Soc.*, 138,
1042 11164-11169, <https://doi.org/10.1021/jacs.6b04338>, 2016.